

<sup>1</sup> On the formation of breakthrough curves tailing  
<sup>2</sup> during convergent flow tracer tests in  
<sup>3</sup> three-dimensional heterogeneous aquifers

---

D. Pedretti, D. Fernàndez-Garcia, Hydrogeology Group, Department of Geotechnical Engineering and Geo-Sciences, Universitat Politècnica de Catalunya UPC-Barcelona Tech, C/Jordi Girona 1-3, Ed.D2/004/01, Barcelona, E-08034, Spain (daniele.pedretti@upc.edu)

D. Bolster, Department of Civil Engineering, University of Notre Dame, USA

X. Sanchez-Vila, Hydrogeology Group, UPC-Barcelona Tech

**Abstract.** Anomalous transport in advection-dominated convergent flow tracer tests can occur due to small-scale heterogeneities in aquifer hydraulic properties. These result in fluctuations of the groundwater velocity field and complex connectivity patterns between injection and extraction wells. While detailed characterization of heterogeneity is often not possible in practice, a proper understanding of what fundamental physical mechanisms can give rise to macroscopic behaviors that are measurable is essential for proper upscaling of solute transport processes. We analyze here how heavy-tailed breakthrough curves can arise in radially convergent flow to a well. The permeability fields are three dimensional multigaussian fields with varying statistical geometry and degrees of heterogeneity. We consider transport of conservative tracers from multiple injection locations by varying distance and angle from the extraction well. Anomalous power law tailing in breakthrough curves is attributed to a variety of features including the initial vertical stratification of the solute that arises due to a flux-weighted injection, the injection distance to the well relative to the depth of the aquifer and the statistics of the heterogeneity field as defined by the correlation length and variance of the permeability. When certain conditions co-occur for a given injection, such as strong connectivity contrasts between aquifer layers, injection distances comparable to the horizontal heterogeneity integral scales and large global variances, breakthrough curves tend to scale as a power-law with unit slope at late time. These findings offer new insights to understand what physical processes must be understood to develop and choose appropriate

<sup>27</sup> upscaling approaches that might reproduce such anomalous transport in het-  
<sup>28</sup> erogeneous advection-dominated systems.

## 1. Introduction

Transport parameters are often obtained from interpreting the temporal evolution of concentrations at a given location or volume control section (breakthrough curves, BTCs). The actual estimated parameters are model-dependent. The conventional approach based on the advection-dispersion equation (ADE, *Bear* [1972]) has been shown consistently to fail at completely predicting data obtained from real sites. In such cases, transport is called 'anomalous' or non-Fickian. Many authors have postulated that non-Fickianity is a consequence of the presence of heterogeneity in hydraulic parameters (e.g. *Levy and Berkowitz* [2003]; *Salamon et al.* [2007]; *Riva et al.* [2008]).

Phenomenological evidence of this effect of heterogeneity comes from observations of heavy-tailed distributions on BTCs (e.g. *Hoehn et al.* [1998]; *Fernández-Garcia et al.* [2004]; *Gouze et al.* [2008]). Sometimes, BTC tails at late times scale like power-laws (PL) of the form  $c \sim t^{-m}$  (long after the peak is observed). The parameter  $m$  is often called the 'BTC slope', since PL distributions scale as straight lines in double log plots; in the literature  $m$  has been reported to range anywhere between 1 and 3 (e.g. *Becker and Shapiro* [2000, 2003]; *McKenna et al.* [2001]).

A general current goal is to find strict relationships between PL-shaped BTCs and specific spatio-temporal distributions of physical soil properties (e.g. *Dentz and Berkowitz* [2003]; *Bijeljic and Blunt* [2006]; *Willmann et al.* [2008]; *Dentz and Bolster* [2010]). In this paper, our aim is to show that heavy-tailed BTCs with PL late-time distributions can be found in finite-scale stationary hydraulic conductivity,  $K$ , fields, provided a third spatial dimension is accounted for and flow is convergent to a well.

50 Convergent flow appears naturally in describing many flow configurations from real  
51 experiments. In fact the most common form of tracer test is perhaps the convergent  
52 flow tracer test (CFTTs). This is for practical reasons, such as a better control of test  
53 duration, reduced required tracer mass and large mass recoveries (compared, for example,  
54 with natural-gradient flow tracer tests).

55 Classical examples of stationary fields include multigaussian fields with log-transformed  
56 hydraulic conductivity. One of the conclusions in *Willmann et al.* [2008] is that no  
57 PL-shaped late-time behavior of BTCs could be observed from transport through two-  
58 dimensional stationary multigaussian fields, unless an artificial modification of the conduc-  
59 tivity field was made. Nonetheless, the presence of heavy-tailed BTCs for short travel dis-  
60 tances in multigaussian fields with log-transformed hydraulic conductivity (called *Y*-field,  
61 where  $Y = \ln(K)$ ) was shown by *Sanchez-Vila and Carrera* [2004] using 1D analytical  
62 and numerical solutions.

63 An example of BTCs that can be observed in heterogeneous media was given by  
64 *Fernàndez-Garcia et al.* [2004], who experimentally studied convergent, divergent and  
65 uniform flow tracer tests in an intermediate-scale three-dimensional heterogeneous aquifer  
66 constructed in the laboratory with different types of sands. The resulting  $K$  distribution  
67 showed correlated structures, well-described by an exponential variogram model. Several  
68 conservative (Bromide) and sorptive (Lithium) tracers were injected at different points  
69 located between one and five horizontal integral scales from the extraction well. Con-  
70 centrations were recorded as depth-integrated BTCs. Four of the experimental BTCs  
71 obtained during the CFTTs using a deep-penetration source injection (*Fernàndez-Garcia*  
72 [2003]) are shown in fig.1 and clearly display non-uniform transport behavior. We observe

73 that: (a) the BTC obtained from injecting at E1 (located two integral scales away from  
74 the pumping well, displayed a heavy-tailed distribution after the peak, well approximated  
75 by a PL with  $m = 1$ ; (b) at the same radial distance from the pumping well, the BTCs  
76 obtained from injections at E2 and E3 were less anomalous and quite symmetric; (c) E4,  
77 also at the same injection distance, is much more irregular and only approximately similar  
78 to a PL with  $m = 1$ .

79 These results lead us to ask the following questions: Does scaling in BTCs with a PL  
80 with  $m = 1$  occur for some specific physical reasons, or is it just a random output? More  
81 generally, are there any, and if so what are the physical mechanisms controlling BTC  
82 scaling, for large time after injection in radial convergent flow?

83 *Willmann et al.* [2008] tried to answer to the latter question, using 2D numerical simula-  
84 tions to reproduce anomalous transport under the assumptions of uniform flow conditions  
85 and finite correlated heterogeneous log conductivity fields (i.e fields with log-normally dis-  
86 tributed hydraulic conductivity). They concluded that classical low-order geostatistical  
87 indicators (such as variograms), usually adopted to characterize these fields, cannot be  
88 directly related to parameters associated with anomalous transport models such as those  
89 including memory functions (*Carrera et al.* [1998]). Similar results were also found by  
90 *Flach* [2012], who used dual-domain models.

91 According to *Zinn and Harvey* [2003] and *Willmann et al.* [2008], among others, connec-  
92 tivity is the hydrodynamic parameter that most influences BTC late-time behavior. Here  
93 connectivity is defined as the ratio between spatially-averaged and effective parameters  
94 defining flow and transport (*Knudby and Carrera* [2006]). We refer to the recent work by  
95 *Renard and Allard* [2013] for an extensive review of connectivity concepts.

96 In the simulations of *Willmann et al.* [2008], the BTC slopes were bounded by a min-  
 97 imum value of  $m \approx 2$ , which is not in agreement with the experimental observations  
 98 reported by *Fernández-García et al.* [2004]. It is not truly fair though to compare these  
 99 works for two main reasons. First, radially converging flow is fundamentally different from  
 100 uniform flow. For instance, tailing can naturally arise in BTCs, even for homogeneous  
 101 fields (*Gelhar and Collins* [1971]; *Moench* [1989]; *Welty and Gelhar* [1994]). Second, two-  
 102 dimensional (2D) models are not suitable to reproduce this type of CFTT, where the  
 103 distance between injection and controlling section is on the range of the representative  
 104 heterogeneity scale such as the integral scale ( $I$ ) in a multigaussian  $K$  field. In this case,  
 105 whenever possible, 3D models are preferable (e.g. *Dagan* [1989]).

106 Dimensionality is also a key factor when studying connectivity. Inclusion models (e.g.  
 107 *Fiori et al.* [2006]) show for instance that non symmetric BTCs naturally arise from the  
 108 distribution of travel times in 3D models under uniform flow; moreover, this method also  
 109 showed that (flow) connectivity is largely enhanced by 3D configurations relative to their  
 110 2D counterparts *Fiori and Jankovic* [2012]. This is particularly true if unconditional  
 111 Sequential Gaussian Simulations (SGS) are used to simulate stochastic hydraulic conduc-  
 112 tivity fields (*Fernández-García et al.* [2010]). In fact, *Willmann et al.* [2008] had to heavily  
 113 condition their simulations to generate highly conductive non-stationary structures that  
 114 gave rise to heavy-tailed BTCs similar to those observed in the field. It should be noted  
 115 that the numerical 3D flow and transport simulations by *Fogg* [1986] showed that one of  
 116 the most influential factors controlling flow and transport is the connectivity of lenses,  
 117 rather than the relative  $K$  value of the lenses themselves. The reliability of 2D SGS to  
 118 adequately reproduce transport connectivity patterns have been extensively debated in

the past (e.g. *Sanchez-Vila et al.* [1996]; *Gomez-Hernandez and Wen* [1998]); however 3D models have received much less study, in large part due to the still highly computationally intensive nature of 3D simulations.

In this paper, we investigated the origin and development of heavy-tailed BTCs using 3D numerical realizations under radially convergent flow conditions. We simulated synthetic heterogeneous fields drawn from a multigaussian lognormal  $K$  distribution. Such a distribution is characterized by different combinations of finite-scale correlation and variances. Our aim was to provide new insights to explain how and why BTCs behave in typical CFTT field settings. We also aimed to find the key physical links to interpret the results obtained from field tracer tests in real applications.

The paper is structured as follows. In Section 2, we described the numerical approach we used to reproduce CFTTs in synthetic heterogeneous aquifers. Section 3 shows the results in which we highlighted how BTC tailing develops in different heterogeneous fields. The paper ends with a final discussion on the similarities between 3D simulations and their corresponding 2D counterparts, the role of the local dispersivity and a possible physical explanation of power-law scaling on the BTCs, in Section 4, and the conclusions.

## 2. Numerical simulation of CFTT in different geological settings

We considered a typical CFTT scenario, in which a passive injection well (or piezometer) is located at a distance ( $r$ ) from an extraction well. We assumed both wells to be fully penetrating the aquifer, which is confined and characterized by constant thickness ( $b$ ). The extraction well is activated to withdraw groundwater at a constant discharge rate ( $Q$ ). Once steady-state conditions are established at the injection well, a known mass ( $M$ ) of tracer is introduced into the aquifer through the injection well. Under ideal conditions

<sup>141</sup> the injected mass is fully recoverable. In real field tests, a combination of mass losses and  
<sup>142</sup> finite recording times leads to partial recovery of the injected mass.

<sup>143</sup> In heterogeneous aquifers, under forced-gradient conditions, the horizontal flow veloc-  
<sup>144</sup> ity can vary along the vertical column by several orders of magnitude. This variability  
<sup>145</sup> depends on the hydraulic disorder of the system (described for instance by variance of Y,  
<sup>146</sup>  $\sigma_Y^2$  which can vary from  $\sigma_Y^2 = 0.1 - 1$  for mildly heterogeneous systems to  $\sigma_Y^2 > 4$  for  
<sup>147</sup> highly heterogeneous ones, e.g. *MacKay et al. [1986]; Bohling et al. [2012]*); it can also  
<sup>148</sup> depend on local hydraulic gradients, which are controlled for instance by well pumping  
<sup>149</sup> rate  $Q$ . Therefore, the amount of tracer mass injected into the aquifer at different depths  
<sup>150</sup> is proportional to the local horizontal velocity found at the different horizons along the  
<sup>151</sup> vertical injection column. This configuration forces one to pose the problem in terms of  
<sup>152</sup> 'flux-averaged' concentration rather than resident ones (e.g. *Parker and Van Genuchten*  
<sup>153</sup> [1984]).

<sup>154</sup> BTCs can be measured both at the extraction well and, if possible, at some control  
<sup>155</sup> section between the injection and the extraction location. We assumed that only the ex-  
<sup>156</sup> traction well is used for measuring concentrations. At the extraction well, concentrations  
<sup>157</sup> are usually observed as 'depth-integrated' measures over the entire screened section of the  
<sup>158</sup> well, taking samples of the water once withdrawn and pushed to the surface. Alterna-  
<sup>159</sup> tively, measurements can be made at different intervals along the screened section of the  
<sup>160</sup> well , for instance using 'clustered columns', or 'packers' (e.g. *Ptak et al. [2004]*). While  
<sup>161</sup> 'depth-integrated' BTCs are more commonly and easily obtained in the practice, 'multi-  
<sup>162</sup> layered' BTC can provide useful information about stratification of transport properties  
<sup>163</sup> of the aquifers, provide valuable potential information about mixing (e.g. *Le Borgne et al.*

<sup>164</sup> [2010]; *Bolster et al.* [2011]) and can help indicate the existence of preferential flow paths  
<sup>165</sup> (e.g. *Ptak and Schmid* [1996]; *Bianchi et al.* [2011]).

<sup>166</sup> With these concepts in mind, we adopted a classical numerical approach consisting of:

- <sup>167</sup> 1. generation of a number of 3D realizations of log hydraulic conductivity  $Y$ -fields from
- <sup>168</sup> a predefined geostatistical model;
- <sup>169</sup> 2. solution of the groundwater flow problem in each of the  $Y$ -fields by setting appro-
- <sup>170</sup> priate boundary conditions to impose forced-gradient behavior to a well;
- <sup>171</sup> 3. solution of the transport problem by means of a random walk particle method and
- <sup>172</sup> 4. calculation of BTCs, both as 'depth-integrated' and 'multilevel' concentrations at
- <sup>173</sup> the well.

<sup>174</sup> Details of the different steps are provided in the subsequent subsections.

## 2.1. Simulation of heterogeneous hydraulic conductivity fields and convergent flow solution

<sup>175</sup> We started by generating three stochastic realizations of  $Y$ -fields using a SGS algorithm  
<sup>176</sup> included in the geostatistical modeling software SGEMS (*Remy et al.* [2009]). The support  
<sup>177</sup> grid consisted of a regular 3D lattice composed of  $N_L=100$  planar layers, each of which  
<sup>178</sup> was made up of  $N_C = 251$  horizontal square cells per side. We used  $i, j$  to identify a  
<sup>179</sup> cell respectively in the  $x, y$  direction ( $i, j = 1, \dots, N_C$ ) and  $k$  to identify a specific layer  
<sup>180</sup> ( $k = 1, \dots, N_L$ ). We assumed  $Y$  to be isotropic in each cell, with the exception of the  
<sup>181</sup> central vertical column, which represented the well. Here we imposed very large vertical  
<sup>182</sup> conductivities. Each cell has unit size, in all three directions (i.e. r=1 corresponds to 1  
<sup>183</sup> cell).

184 By construction, all  $Y$ -fields had zero mean log-transformed hydraulic conductivity  
 185 ( $\bar{Y} = 0$ ). Three exponential variograms with unit variance ( $\sigma_Y^2 = 1$ ) and variable integral  
 186 scales ( $I$ ) were used. Thus, denoting the three directional integral scales as  $I_x, I_y$  and  $I_z$ ,  
 187 we built:

- 188 • Field (A):  $I_x = I_y = I_z = 4$ ;
- 189 • Field (B):  $I_x = I_y = 40$ ,  $I_z = 4$ ;
- 190 • Field (C):  $I_x = I_y = I_z = 40$ .

191 Field (B), reported on the left of fig.2, displays statistical axisymmetric anisotropy, with  
 192 ratios  $I_x = I_y$  and  $I_x/I_z = I_y/I_z = 10$ . Field (A) and (C) are statistically isotropic, but  
 193 with different integral scales to explore the impact of the relative distance of the injection  
 194 point. Note that the same fields will be used throughout to explore the effect of having  
 195 larger variances (increased degree of heterogeneity) by simple scaling of the variance. For  
 196 this reason fig. 2 does not report a color legend.

197 To obtain pumping conditions in each heterogeneous field, we proceeded as follows. In  
 198 each realization and at each cell,  $Y$  were back-transformed to arithmetic values ( $K =$   
 199  $\exp(Y)$ ), and set as the hydraulic conductivity within the finite-difference numerical code  
 200 Modflow-2000 (*Harbaugh et al. [2000]*). Flow simulations were run under steady-state  
 201 conditions and the aquifer was considered confined. To simulate radial flow conditions,  
 202 we set Dirichlet boundary conditions at the lateral domain sides, and assigned a sink  
 203 term to the bottom cell of the pumping well, situated at the center of the domain. Flow  
 204 effects in the pumping well were achieved by setting a large anisotropy ratio in the local  
 205 hydraulic conductivity between horizontal and vertical direction ( $K_z/K_x = 10^5$ ) in the  
 206 pumping well central column.

Finally, to simulate other  $Y$ -fields, characterized by the same heterogeneous architecture but different variances, we multiplied each cell of the  $Y$ -field by a factor of 2 and  $2\sqrt{2}$  to obtain new synthetic fields with variances of  $\sigma_Y^2=4$  and 8 respectively for fields (A),(B) and (C). No numerical convergence problems were found regardless the variance used.

## 2.2. Design of 3D transport simulations and estimation of depth-integrated BTCs

We simulated conservative solute transport using the random-walk particle-tracking code RW3D (*Fernàndez-Garcia et al.* [2005]; *Salamon et al.* [2006]) which is efficiently coupled with Modflow-2000. In this algorithm,  $M$  is discretized into  $N_p$  particles (the mass of each particle being  $m_p = M/N_p$ ). Based on the Langevin equation, each particle moves with a drift displacement, based on the radial flow velocities calculated at each cell of the domain by Modflow-2000, and a Brownian motion that accounts for local dispersive process. In our simulations, we set a constant porosity value of  $\phi = 0.1$  in all simulations and  $N_P = 3 \cdot 10^4$ . Via a convergence test we found our results to not be sensitive to an additional number of particles.

Injection wells were located at 16 different points in the domain around the extraction well as depicted in fig. 2. Each tracer test was independent of all others. The injection positions were oriented along the coordinate axes and were defined such that

- injection boreholes at points U1,R1,L1,D1, located at  $r = 5$  from the extraction well,;
- injection boreholes at points U2,R2,L2,D2, located at  $r = 12.5$  from the extraction well;
- injection boreholes at points U3,R3,L3,D3, located at  $r = 25$  from the extraction well;

<sup>228</sup> • injection boreholes at points U4,R4,L4,D4, located at  $r = 75$  from the extraction  
<sup>229</sup> well;

<sup>230</sup> In all simulations, we started by setting an isotropic local dispersivity value of  $\alpha =$   
<sup>231</sup> 0.25, which ensures an  $r/\alpha > 20$  at the injection locations. This was chosen considering  
<sup>232</sup>  $r/\alpha = 20$  as a suitable minimum value to ensure advection-dominated transport in radial  
<sup>233</sup> flow problems in homogeneous aquifers (e.g. *Moench* [1989]). We considered  $\alpha$  to be  
<sup>234</sup> isotropic in all directions (i.e.  $\alpha_L=\alpha_T=\alpha_Z$ , where  $L, T, Z$  indicate here the directions,  
<sup>235</sup> respectively collinear, transverse in the plane and transverse in the vertical direction with  
<sup>236</sup> the main flow direction), to avoid a possible bias in the interpretation of our results due  
<sup>237</sup> to local anisotropic dispersive mechanisms.

<sup>238</sup> The number of particles in each layer was taken to be proportional to the local Darcy  
<sup>239</sup> flux, to better represent flux-averaged conditions. Particles were introduced in the system  
<sup>240</sup> from layer  $k=5$  to layer  $k=95$ . Five cells were left empty at the top and at the bottom, to  
<sup>241</sup> avoid rebounds and other uncontrolled boundary effects. Injection took place as a pulse,  
<sup>242</sup> at the initial time ( $t = 0$ ).

<sup>243</sup> We obtained 'depth-integrated' BTCs after estimating the density of the distribution  
<sup>244</sup> of travel times of the ensemble of released particles. As such, we did not keep track  
<sup>245</sup> of where (at which depth) particles were injected. Since each particle carries the same  
<sup>246</sup> amount of mass ( $m_p$ ), the estimated density distribution of travel time was equivalent to  
<sup>247</sup> the estimation of a normalized BTC.

<sup>248</sup> The estimation of the density function was based on the automatic optimal kernel den-  
<sup>249</sup> sity estimator algorithm described by *Fernàndez-Garcia and Sanchez Vila* [2011]. The  
<sup>250</sup> numerical solution was successfully tested under homogeneous conditions against the an-

<sup>251</sup> alytical formulae of *Moench* [1989] and *Gelhar and Collins* [1971], to ensure measured  
<sup>252</sup> transport was not affected by boundary conditions.

### 2.3. An illustrative result of a depth-integrated BTC

<sup>253</sup> Let us first analyze some key aspects involved in the formation of a BTC obtained in  
<sup>254</sup> one specific simulation. This is done to highlight the main phenomenological features  
<sup>255</sup> needed to understand subsequent results. As our example, we considered injection at  
<sup>256</sup> location L4 in field (B) (fig. 2) with  $\sigma_Y^2 = 4$ . Fig. 3 is divided in four subplots, each  
<sup>257</sup> of them representing the position of 1000 particles (above) and the 'depth-integrated'  
<sup>258</sup> BTCs (below) collected at the well at different times ranging from the initial injection  
<sup>259</sup> time to a late time when the vast majority of particles have been captured at the well.  
<sup>260</sup> The background colors represent the distribution of the (log)hydraulic conductivities on  
<sup>261</sup> the vertical section parallel to the x-axis, passing through both the injection and the  
<sup>262</sup> extraction wells. Note that a consistent system of units was used throughout this work.

<sup>263</sup> At the initial time particles are concentrated in the highly conductive areas along the  
<sup>264</sup> vertical section where Darcy velocities are higher (red pixels) while only a few particles  
<sup>265</sup> are located in less conductive areas (green pixels).

<sup>266</sup> At the first earlier intermediate time, particles located initially within the higher  $Y$ -  
<sup>267</sup> zones have traveled greater distances, eventually reaching the extraction well, compared  
<sup>268</sup> to those located in initially lower permeability areas. Since a large number of particles  
<sup>269</sup> were initially injected in relatively high  $Y$  areas, the concentration peak appears at a  
<sup>270</sup> relatively early time.

<sup>271</sup> At the second intermediate time, most of the particles (i.e. mass) have been collected,  
<sup>272</sup> and only a few remain in the system. Note that the BTC scales very differently before and

273 after this time. In particular, a fairly well-defined tail with behavior similar to  $c \sim t^{-1}$  is  
 274 clearly visible from this moment on.

275 This example indicates that our numerical settings were able to produce anomalous  
 276 transport which gives rise to heavy-tailed BTCs, similar to experimental observations.  
 277 See for example fig. 3 as compared to case E1 case in fig. 1. We could therefore take  
 278 advantage of the numerical model to see whether we could provide a physical explanation  
 279 for  $m \approx 1$ . To address this issue in detail, which will be more thoroughly discussed in  
 280 Section 4, we studied the impact of imperfect stratification in the 3D model.

## 2.4. Simulation of 'multilevel' transport

281 To evaluate the variability of solute mass arriving at different depths in a fully pene-  
 282 trating pumping well we propose the following approach, which is graphically summarized  
 283 in fig. 2. We noted that in radial convergent flow, planar flow is dominant with respect  
 284 to vertical flow. Moreover, at relatively short injection distances compared with the  
 285 horizontal integral scales, plumes in each planar layer migrate practically independently  
 286 from those in other planar layers. This effect is enhanced in fields displaying axisymmetric  
 287 anisotropy. Fig. 3 illustrates this behavior, where it was found that particles move mainly  
 288 horizontally.

289 Noting that negligible vertical velocities and transverse dispersion lead to particle paths  
 290 that follow primarily the horizontal plane in which particles are initially injected, we  
 291 proceeded as follows. We separated each  $k$  layer making up the 3D block and use them  
 292 as independent 2D  $Y$ -fields. The new 2D fields have 251 cells per side with unit thickness  
 293 ( $b = 1$ ). They have the same horizontal integral scales  $I_x, I_y$  but, due to the effects of  
 294 sub-sampling, (slightly) smaller variance than the original 3D  $Y$ -field (e.g. from  $\sigma_Y^2 \approx 4$

in the 3D simulations to an average value of  $\sigma_Y^2 \approx 3.5$  for the 2D simulations). We did not re-normalized the variance in each layer to obtain the same original value as the 3D simulation since our aim was to evaluate the effects of the stratified transport in each layer within the 3D formation and asked how much information does one obtain from 2D vs the full 3D system?

In each of the  $N_k = 100$  layers, we calculated 2D flow and transport and estimated BTCs, using the same procedure described in previous sections. We injected the same mass ( $M$ ) per layer as a pulse release directly at the same 16 positions used for the 3D simulations. In each layer, we imposed the same discharge rate as in the 3D counterparts ( $Q$ ). We thus obtained 100 BTCs (one for each layer) for each injection position; we call BTCs obtained from this approach '2D-BTCs'.

As an illustrative example, we considered again the injection taking place at location L4 in field (B) with  $\sigma_Y^2 = 4$ . In fig. 4 the 'depth-integrated' BTC obtained from 3D transport (fig. 3, bottom-right) is depicted as a thick, black line. Along with that, the gray curves represent the 100 BTCs obtained after injecting in each layer making up the 3D block (i.e. the 2D BTCs). We note from fig. 4 that, unlike the 3D integrated case, 2D-BTCs never show heavy power-law tailing, but are mostly symmetric. This means that the behavior of most of these BTCs is much more similar to that of a homogeneous  $Y$  field rather than the typical curves in heterogeneous media. Moreover, 2D-BTCs look like 'convolved' versions of one another, as indicated by the spread of the maximum peak of concentrations on each BTC (marked by a blue square). This behavior is qualitatively very similar to the one found by *Becker and Shapiro* [2003], where they reproduced depth-integrated BTCs

<sup>317</sup> as a convolution of independent BTC obtained from transport in individual channels. We  
<sup>318</sup> discuss and compare their results with ours in Section 4.

<sup>319</sup> The difference between the estimated concentration for 2D and 3D BTCs is due to  
<sup>320</sup> the fact that in 2D realizations the injected mass is equal to the total injected mass for  
<sup>321</sup> the 3D cases, while in each layer of the 3D simulations mass enters as a flux-weighted  
<sup>322</sup> amount. In addition, to compare different BTCs, we need to express variables in terms  
<sup>323</sup> of dimensionless parameters. To this end we used the following dimensionless quantities:

- A estimated mass density,  $\hat{p}(t, k)$ , was obtained by

$$\hat{p}(t, k) = \frac{1}{D_F(k)} \frac{QC(t)}{\int QC(t)dt} \quad (1)$$

where  $D_F$  is a dilution factor that is proportional to the mass injected in the system at each layer in 2D simulations and the 3D simulations.  $C(t)$  is the resident concentration at the well locations.  $D_F$  can be defined as

$$D_F(k) = \frac{q_x(k)}{\sum_{k=1}^{N_L} q_x(k)} \quad (2)$$

<sup>324</sup> where  $q_x(k)$  is the local seepage velocity at each injection location.

<sup>325</sup> • A normalized time ( $t_c$ ) was defined such that

$$t_c = \frac{t}{t_{adv}} \quad (3)$$

<sup>326</sup> where  $t_{adv}$  is the advection time (e.g. Moench [1989]), such that

$$t_{adv} = \frac{\pi r^2 b \phi}{Q} \quad (4)$$

<sup>327</sup> where  $b$  is the aquifer thickness ( $b = 1$  for 2D simulations and  $b = 100$  for 3D simulations).

<sup>328</sup> This normalization ensures that the concentration peaks of the BTCs under CFTTs per-

<sup>329</sup> formed from injection locations at different distances ( $r$ ) from the pumping well always  
<sup>330</sup> collapse around  $t_c = 1$  for homogeneous aquifers.

<sup>331</sup> • A normalized injection distance ( $r_\lambda$ ) was obtained to compare BTCs obtained from  
<sup>332</sup> different realizations with different integral scales. We normalized  $r$  by the horizontal  
<sup>333</sup> integral scale of each field,  $I_x$ , such that

$$r_\lambda = \frac{r}{I_x} \quad (5)$$

<sup>334</sup> • A normalized vertical injection length ( $L_z$ ) was obtained to measure 'how stratified'  
<sup>335</sup> the solute is injected into the system, and thus how homogenized the solute transport  
<sup>336</sup> is for short travel distances.  $L_z$  was found as the ratio between the aquifer thickness ( $b$ ,  
<sup>337</sup> which also corresponds to the particle injection length) and the vertical integral scale  $I_z$ ,  
<sup>338</sup> such as

$$L_z = \frac{b}{I_z} \quad (6)$$

<sup>339</sup> Note that in Eq.(4), we used  $r$  rather than  $r_\lambda$ , since we wanted to emphasize the effect  
<sup>340</sup> of heterogeneity on the solute travel time.

<sup>341</sup> Let us first analyze the case when  $D_F$  was not accounted for and the same mass was  
<sup>342</sup> injected in each 2D simulation and equal to the one imposed for the 3D simulations ( $M$ ).  
<sup>343</sup> This is plotted in fig. 4 - I (big window) from which we can infer two fundamental issues.  
<sup>344</sup> First, it looks like 2D settings are not suitable to reproduce anomalous transport, even  
<sup>345</sup> though the 2D simulations were performed with similar horizontal variogram statistics  
<sup>346</sup> (e.g. same correlation lengths but slightly smaller variance) as the 3D counterparts.  
<sup>347</sup> We believe this is due to the use of unconditional 2D SGS simulations, a result that is

<sup>348</sup> similar to what was observed by *Willmann et al.* [2008]. Second, the ensemble of peak  
<sup>349</sup> concentrations for the 2D BTCs (indicated by squares in fig. 4) scale like a PL with unit  
<sup>350</sup> slope, i.e. of the form  $\hat{p}(t) \sim t_c^{-1}$ .

<sup>351</sup> We also observe the effect of rescaling particle density with  $D_F$ . This is plotted in  
<sup>352</sup> 4 - II (small window), where to avoid redundancy we only plot the 2D-BTC peaks. It  
<sup>353</sup> can be seen that the concentration peaks were found at similar concentrations to the  
<sup>354</sup> 3D counterparts. This confirms that the mass distribution among layers can perhaps be  
<sup>355</sup> thought of as a convolution of effects giving rise to such tailing (i.e. as in *Becker and*  
<sup>356</sup> *Shapiro* [2003]). There is not an exact match between the 2D peaks and 3D curves (as  
<sup>357</sup> it would be expected for instance analyzing multilevel concentrations at the well) due to  
<sup>358</sup> intrinsically different flow structures of the 2D and 3D flow simulations.

<sup>359</sup> In the next section we present the most relevant findings extracted from the additional  
<sup>360</sup> simulations, in order to find the impact of the degree of heterogeneity on the different late  
<sup>361</sup> time slopes of the BTCs.

### 3. Comparison of different cases

<sup>362</sup> Here we describe other significant results of our numerical analysis, which we compared  
<sup>363</sup> with the illustrative example in fig. 4. The goal was to show how exportable the scaling  
<sup>364</sup>  $\hat{p}(t) \sim t_c^{-1}$  of the depth-integrated BTC tailing at late times is. We also aimed to link this  
<sup>365</sup> slope to some characteristic physical patterns to gain a proper physical understanding of  
<sup>366</sup> why and when it occurs.

### 3.1. Evaluation of the anisotropic case (field B) with $\sigma_Y^2=4$

367 In this part, we compare the results for other injection locations within the anisotropic  
 368 field (B) with  $\sigma_Y^2=4$ . For this field the normalized injection length was  $L_z=25$ .

369 In addition to the injection at L4, in fig. 5 we plot the results for three other injection  
 370 locations, specifically at L1, L2 and L3. These cases look at injections at different distances  
 371 from the pumping well. In this figure, the depth-integrated BTCs (black line) are reported  
 372 along with a cloud of points representing the peaks of the 2D BTC simulations, which  
 373 were obtained using the 'layer decomposition' approach described above.

374 We observe that the depth-integrated BTCs always show some form of heavy-tailed dis-  
 375 tribution, but that the BTC slopes change as the injection location  $r_\lambda$  increases. Specifi-  
 376 cally, we observe that injections at short distances (L1,L2) where the normalized injection  
 377 distance is small ( $r_\lambda \approx 0.1, 0.3$ ), tailing is observed with constant slope, but different from  
 378 (faster than)  $\hat{p}(t) \sim t_c^{-1}$ . This regime is on the other hand clearly observed at the largest  
 379 injection distance (L4), where  $r_\lambda \approx 1.8$ . A subtle look at the data suggests that a regime  
 380 qualitatively like  $\hat{p}(t) \sim t_c^{-1}$  may exist to some extent in all cases, but persists for much  
 381 longer times as the injection distance approaches  $r_\lambda \approx 1.8$ .

382 Looking at the 'cloud' of 2D peaks, it seems that they align well with  $\hat{p}(t) \sim t_c^{-1}$  for all  
 383 injection locations. However, it is visually evident that the relative spread of these point  
 384 varies, being narrowest at L1 and widest at L4, with L2 and L3 as intermediate cases. To  
 385 quantify this spread, we calculated the spread of this 'cloud', defining

$$\sigma_t^2 = \frac{1}{N_k - 1} \sum_{k=1}^{N_k} \left( \left| \log(t_{pk}(k)) - \overline{\log(t_{pk})} \right| \right) \quad (7)$$

386 where  $\log(t_{pk})$  represents the base 10 log-transformed value of the dimensionless time  
 387 coordinate at which the peaks are observed.  $\overline{\log(t_{pk})}$  is the average of log-transformed  
 388 dimensionless peak times over the  $N_k$  layers. A low value for this spread (e.g.  $\sigma_t^2 \rightarrow 0$ )  
 389 would indicate that transport is very similar in all the horizons (e.g. relatively homoge-  
 390 neous medium), while large variances represent stronger heterogeneity induced spreading.

391 For injection location L1,  $\sigma_t^2 = 0.076$ . This low value is due to the relatively short  
 392 injection distance, which prevents the tracer from displaying strong vertical stratification  
 393 of the concentration measurable in terms of 'depth-integrated' BTCs. At L2 and L3,  
 394  $\sigma_t^2=0.165$  and 0.324, respectively, emphasizing the development of vertical stratification  
 395 of the plume, and enhanced differences between layers. At L4, where  $r_\lambda$  is close to the  
 396 horizontal integral scale,  $\sigma_t^2 = 0.561$ , indicating that the plume is more stratified than in  
 397 the other cases, and is heavily controlled by the different properties of each layer.

398 Note two fundamental points. Anomalous tailing like  $\hat{p}(t) \sim t_c^{-1}$  clearly takes place (1)  
 399 when the solute travel distance is of the order of the horizontal heterogeneous scale of the  
 400 multigaussian field (i.e.  $R$  of the order of  $I_X$ ); and (2) when  $\sigma_t^2$  is maximum among the  
 401 four injection points L1 to L4. As shown in the following sections, these characteristic  
 402 patterns will be also found for the other field geometries and variances.

### 3.2. Comparison with isotropic fields

403 Noting that field (B) (fig.2) has an anisotropic correlated structure of hydraulic con-  
 404 ductivity, a reasonable question is whether the stratification of the plume is controlled  
 405 dominantly by the stratified distribution of  $Y$ . We therefore evaluated the behavior of  
 406 BTCs for the 2D and 3D  $Y$  fields associated with fields (A) and (C), which are isotropic.

The curves for field (A) are plotted in fig. 6. For this case, the normalized injection distance is again the same as for field (B), i.e.  $L_z = 25$ . We plot only the curves corresponding to injection wells R1 to R4, since the other arrays (L,U,D) display similar behavior. As  $I_x = 4$  in this field, the normalized injection distance is close to unity for R1 ( $r_\lambda \approx 1.8$ ) and increases up to  $r_\lambda \approx 18$  for R4. At position R1, 3D BTCs display anomalous tailing with a behavior very similar to  $\hat{p}(t) \sim t^{-1}$  right after its peak. As soon as the injection distance increases, this behavior seems to diminish, until it is no longer truly observable at R4.

Observing the peaks distribution, the spread at R1 is larger ( $\sigma_t^2 = 0.621$ ) than at R2 and R3 ( $\sigma_t^2 = 0.372$ ). At R4, since no tailing develops, one expects  $\sigma_t^2$  to be the smallest value; however it is slightly higher than for the other cases (0.717). It should be noted from fig. 6 that this latter value can be biased by the presence of a few outliers (a few layers displaying very large peak time). Disregarding the 5 largest values at peak times (5% of the total number of layers) leads  $\sigma_t^2$  to reduce to 0.341, which is smaller than for R1, R2, and R3.

The curves for field (C) are plotted in fig. 7. In this case,  $L_z = 2.5$ , which means more homogenization in the BTCs might be expected. We find that, at very short normalized injection distances, such as R1 ( $r_\lambda = 0.1$ ), no heavy-tailed behavior is clearly observed in the 3D BTC, while a tailing behavior emerges once again as the normalized injection distance increases to order one and a broad time range of peak arrival times occurs: e.g. at R4 ( $r_\lambda = 1.8$ ), BTC scales as  $\hat{p}(t) \sim t_c^{-1}$ . Again, field (C) displays a similar behavior as in the other field (A) and (B). The distribution of 2D peaks is very narrow when no

<sup>429</sup> tailing develops (at R1  $\sigma_t^2 = 0.07$ ), and it is the largest among the four injection location  
<sup>430</sup> at R4 ( $\sigma_t^2 = 0.25$ ).

<sup>431</sup> We found in BTCs from field (A) and (C) a similar behavior as the one found on  
<sup>432</sup> BTCs for field (B). Accounting for the 2D-peak outliers values at R4 in field (A), the  
<sup>433</sup> new observations suggest again that  $\hat{p}(t) \sim t_c^{-1}$  is observed in the 3D BTC when  $\sigma_t^2$  is the  
<sup>434</sup> largest among the four injection point in each field and  $r_\lambda \approx 1$  is met.

<sup>435</sup> The similar behavior between BTCs from the isotropic fields (A) and (C) and BTCs  
<sup>436</sup> from stratified field (B) can be explained considering the initial vertical stratification of  
<sup>437</sup> the tracer, which is quite relevant and independent of the statistical structure of the  
<sup>438</sup> media in our single realization analysis. It seems that, if the solute travel distance is very  
<sup>439</sup> small compared with the injection distance, the system acts as practically homogeneous  
<sup>440</sup> and solutes tend to arrive at similar times, while if the solute travel distance is very  
<sup>441</sup> large, transport becomes more homogenized, as the solute samples a sufficient number of  
<sup>442</sup> heterogeneous scales before being collected at the well.

### 3.3. Effect of changing the injection location

<sup>443</sup> In single stochastic realizations and particularly under radial flow conditions, solute  
<sup>444</sup> behavior is hardly ergodic. Non ergodicity of the plume means that BTCs can vary  
<sup>445</sup> drastically from realization to realization. A direct consequence of ergodicity would be  
<sup>446</sup> that all curves would not depend on the specific injection location, but only on its distance  
<sup>447</sup> to the well. In our realizations, this is clearly not the case, and so we compared solutions  
<sup>448</sup> obtained for the BTCs recorded at points located at the same injection distance from  
<sup>449</sup> different directions.

450 Referring to fig.2 for the position map, we plot in fig. 8 the depth-integrated BTCs and  
 451 relative 2D peaks obtained for locations D2 , L2 , D4 and L4 for all three fields (A),(B),  
 452 and (C). For these simulations, we kept  $\sigma_Y^2=4$ .

453 For field (A) we observe that the shapes of the BTCs are slightly different for injection  
 454 locations L2 and D2 ( $r_\lambda \approx 3$ ) and no PL tail is observed. At L4 ( $r_\lambda \approx 18$ ), BTCs show a  
 455 well-defined  $\hat{p}(t) \sim t_c^{-1}$  at late times; here, the spread of the distribution of 2D peaks is  
 456 close to the unity ( $\sigma_t^2$  at L4 = 0.701). At D4, the variance is slightly smaller than in the  
 457 previous case ( $\sigma_t^2=0.533$ ), and analogously to what is seen for R4 (fig. 6), the BTC does  
 458 not scale with  $\hat{p}(t) \sim t_c^{-1}$  (see fig. 6).

459 Looking now at the results from field (B), the late-time behavior of BTCs at D2 and  
 460 L2 ( $r_\lambda \approx 0.6$ ) is practically the same, showing no constant PL tailing. Here, the spread  
 461 of the distribution of 2D peaks is narrow ( $\sigma_t^2 = 0.263$  for D2 and  $\sigma_t^2 = 0.165$  for L2),  
 462 indicating that once again the BTC does not develop for low vertical variability of the  
 463 plume behavior. A more pronounced PL effect is found at D4, but not in the case of  
 464 injection from L4. Again, despite the fact that both injection points are located at  $r_\lambda \approx$   
 465 1.8, the spread of the 2D peaks distribution is much higher for D4 ( $\sigma_t^2=1.007$ ) than at L4  
 466 ( $\sigma_t^2=0.562$ ).

467 In field (C) (right), for injection locations D2 and L2 and L4, BTCs are found to follow  
 468 a relatively similar symmetric behavior at late time. Only at D4 the BTC shows a more  
 469 non symmetric distribution (roughly following  $\hat{p}(t) \sim t_c^{-1}$ , despite the presence of multiple  
 470 peaks) Once again, the spread of the peaks is higher when BTCs display less symmetric  
 471 distributions and more tailing ( $\sigma_t^2 = 0.252$  at D4) than where no tailing occurs ( $\sigma_t^2 = 0.045$   
 472 at D2;  $\sigma_t^2 = 0.036$  at L2;  $\sigma_t^2= 0.056$  at L4).

473 These results serve to highlight and confirm the previous hypothesis, i.e. that a combi-  
 474 nation of high  $\sigma_t^2$  and  $r_\lambda$  close to unity to determine  $\hat{p}(t) \sim t_c^{-1}$ , independent of injection  
 475 location and type of geological setting. It should be noticed that the characteristic values  
 476 of  $\sigma_t^2$  for tailing to develop vary from field to field. It is difficult at this level to build a  
 477 general rule, if it exists, to quantitatively evaluate what this value should be for  $\hat{p}(t) \sim t_c^{-1}$   
 478 to develop. For this purpose, additional numerical outcomes were needed. We address  
 479 such an evaluation in the last Section.

### 3.4. Effect of $Y$ variance

480 We explore here the effect of the variance of the log-transformed hydraulic conductivity,  
 481  $\sigma_Y^2$ , on the BTC tailing. In our analysis, we focused on values of  $\sigma_Y^2=1, 4$ , and  $8$ . For illus-  
 482 trative purposes we will use the example of anisotropic field (B) (fig.2 b), with injections  
 483 from two different locations (L2 and L4). Again, these are chosen to illustrate results and  
 484 it is important to note that similar behavior was observed and conclusions made with  
 485 observations from the other fields and locations. The results are displayed in fig. 9.

486 As one might intuitively expect, the general effect of increasing  $\sigma_Y^2$  is to increase  $\sigma_t^2$ . At  
 487 L2, we observe that the variance of the 2D peaks increases from  $\sigma_t^2=0.038$  for  $\sigma_Y^2=1$  to  
 488  $\sigma_t^2=0.329$  for  $\sigma_Y^2=8$ . In none of the BTCs do we observe  $\hat{p}(t) \sim t_c^{-1}$ , which we attribute to  
 489 the fact that injections take place very close to the well, and our hypothesized condition  
 490  $r_\lambda$  close to unity is not met.

491 At L4 (where  $r_\lambda \approx 1.8$ ), BTCs are more anomalous. While for  $\sigma_Y^2=1$ , with  $\sigma_t^2=0.143$ ,  
 492 BTCs do not show a clear PL behavior, this is much more visible for the larger variance  
 493 cases of  $\sigma_Y^2=4$  and  $8$ , where  $\hat{p}(t) \sim t_c^{-1}$  at the late time. In the two latter cases,  $\sigma_t^2$  is  $0.562$   
 494 and  $1.101$  respectively.

495 From this last analysis, we observe that the variance of log conductivity is a key con-  
 496 trolling factor in the development of PL tailing on our BTCs. In particular though, these  
 497 results provide evidence confirming our two other hypothesized conditions for  $\hat{p}(t) \sim t_c^{-1}$ ,  
 498 which are (1) an injection distance close to the integral scale and (2) a large spread of the  
 499 2D peaks.

#### 4. Discussion

500 From our results, we observed so far that in many cases that meet certain conditions,  
 501 a PL behavior of the form  $\hat{p}(t) \sim t_c^{-1}$  develops on depth-integrated BTCs when collected  
 502 during CFTTs in advection-dominated aquifers. This behavior is highly variable, but we  
 503 identify common patterns to phenomenologically explain this behavior. In particular, we  
 504 note that for  $\hat{p}(t) \sim t_c^{-1}$  to take place on BTCs, the normalized injection distances should  
 505 be  $r_\lambda \approx 1$ . If it is much smaller or much larger than this it will not occur, although  
 506 BTCs may still be highly non symmetric. Once this condition is met, the PL extends  
 507 over larger time ranges with increasing  $\sigma_Y^2$ , or better said larger  $\sigma_t^2$ , which is controlled  
 508 by  $\sigma_Y^2$ . Peak times have been already reported in the literature to characterize flow and  
 509 transport variables (e.g. *Bellin and Rubin* [2004]); here, we can attribute a large  $\sigma_t^2$  to  
 510 large variability of point-to-point connectivity patterns (e.g. *Trinchero et al.* [2008]) along  
 511 the vertical injection line.

512 We note that the presented findings are based on a finite set of realizations and caution  
 513 should be taken in trying to generalize them. However, based on our observations, there  
 514 are some questions we would like to address here: (1) Is there, and if so, how strong is the  
 515 correlation between 2D peak spreading and 3D tailing in our simulations? (2) Does local  
 516 dispersivity play a key role in 3D tailing and/or 2D peak spreading? (3) Can we explain

517 tailing a with unit slope on both 2D peak distributions and in late-time 3D BTCs? We  
 518 provide answers in the following.

#### 4.1. How peak spreading and tailing can be related?

519 We observe that the peak spreading, measured by  $\sigma_t^2$ , has to surpass some critical  
 520 threshold for the behavior  $\hat{p}(t) \sim t_c^{-1}$  on the BTC to occur, but so far we have only  
 521 qualitatively indicated that  $\sigma_t^2$  has to be generally 'large' for this regime to take place.  
 522 It would be useful to find a more quantitative relationship between this value and some  
 523 parameters it may depend on.

524 We started to compare if peak spreading can be related with the non symmetric degree  
 525 of the 3D BTCs. Tailing has been seen to be highly variable from case to case, and peak  
 526 distribution is in addition non unique between different types of fields. Let us focus one  
 527 moment only on those injection locations providing conditions for the 3D BTCs to display  
 528  $\hat{p}(t) \sim t_c^{-1}$ . As indicated in Section 3.2, this condition takes place for field (A) at  $R1$ ,  
 529 where  $\sigma_t^2 = 0.621$ , for field (B) at L4, where  $\sigma_t^2 = 0.561$ , and for field (C) at R4, where  
 530  $\sigma_t^2 = 0.25$ . Note that a value of  $\sigma_t^2 = 0.25$ , which is sufficient for field (C) to generate  
 531  $\hat{p}(t) \sim t_c^{-1}$ , is not sufficient for field (B), as in the latter field it would correspond to an  
 532 intermediate injection point between L2 and L3, which do not show such a well-defined  
 533 power-law behavior. However, L2 and L3 still display anomalous behavior.

534 We explore here, for each field (A),(B) and (C) and for all the system variances ( $\sigma_Y^2 =$   
 535  $1, 4, 8$ ), whether a relationship can be built between peak spreading and the non-symmetric  
 536 behavior of 3D BTCs at least for those injection points that satisfy the  $r_\lambda \approx 1$ . We plot  
 537 in fig. 10, for each of these points, the corresponding peak spreading distance ( $\sigma_t^2$ ) and  
 538 another characteristic distance ( $\beta$ ) indicating the degree of tailing of the corresponding 3D

539 BTC. The latter was calculated as the normalized distance between the peak concentration  
 540 time of the 3D BTC ( $t_{pk}$ ) and the first moment of the travel time distribution ( $\bar{t}$ ) such  
 541 that

$$\beta = \frac{t_{pk} - \bar{t}}{\bar{t}}. \quad (8)$$

542 Note that a value of  $\beta \rightarrow 0$  indicates that the peak time corresponds to the center of  
 543 mass of the distribution, which means a symmetric distribution, similar for instance to  
 544 the BTC modeled under homogeneous conditions.

545 Results are shown in fig. 10. In field (A) the points that satisfy the required condition  
 546  $r_\lambda \approx 1$  correspond to injection locations R1,U1,D1,L1. For field (B) and field (C), on  
 547 the other hand, these injection locations are R4,U4,D4,L4. In fig. 10 it can be seen that  
 548 there is a good correlation between  $\sigma_t^2$  and  $\beta$ , but there is a striking difference between  
 549 the behavior of points in field (A) (using the local dispersivity value of  $\alpha = 0.25$ ) and the  
 550 ones in fields (B) and (C). In the first case, points at (A) with  $\alpha = 0.25$  are distributed  
 551 very similarly to a power-law function of the form  $\sigma_t^2 \propto \beta^{0.5}$ . For the other case, if we  
 552 exclude the some outliers (such as the point indicated by 'N') in the plot, points (B) and  
 553 (C) seem to be still power-law distributed, but this time of the form  $\sigma_t^2 \propto \beta^2$ . This  
 554 result reveals several important aspects.

555 First: we observe that for field (A) with  $\alpha = 0.25$ , a short increase of the 2D peak  
 556 variance (i.e. higher independent behavior of strata in the domain) leads to higher tailing,  
 557 while this regime is much slower for fields (B) and (C) (i.e. more variability between strata  
 558 is needed on field (B) and (C) to generate the same amount of non symmetric behavior  
 559 as in the field (A)).

560 Second: the plot suggests that the behavior for field (B) and field (C) is very similar,  
 561 despite the characteristic vertical injection distance  $L_z$  being an order of magnitude larger  
 562 in field (B) than in field (C). This means that in this configuration, solute initial stratifi-  
 563 cation due to the flux-weighted injection mode dominates, on single realizations, over the  
 564 statistical distribution of  $Y$ .

565 Third: the plot quantitatively suggests how total variance ( $\sigma_Y^2$ ) controls the distribution  
 566 of peak time ( $\sigma_t^2$ ) and in turn the nonsymmetric degree of the 3D BTC ( $\beta$ ). As one might  
 567 expect, this figure intuitively suggests that the larger the total variance in 3D simulations,  
 568 the larger the difference in connectivity displayed by the different layers of the formation,  
 569 and the larger the effect of stratification.

#### 4.2. Are results sensitive to the local dispersivity?

570 All simulations presented so far have an isotropic local dispersivity  $\alpha = 0.25$ . This  
 571 value was set to enforce that dimensionless parameter  $r/\alpha > 20$  and maintain advection-  
 572 dominated transport. Another similar important dimensionless parameter that might play  
 573 an important role is

$$I_\alpha = \frac{I}{\alpha}, \quad (9)$$

574 which can be thought of as a Peclet number. Typically, large  $I_\alpha$  suggests advection-  
 575 dominated transport, while low values represent dispersion-dominated regimes. In our  
 576 simulations, fields (B) and (C) have  $I_\alpha = 160$  (considering  $I = I_x$  in field (B)), while field  
 577 (A) only has  $I_\alpha = 16$ . Note that the two correlations empirically suggested in Fig 10  
 578 discriminate field (A) with fields (B) and (C), which may suggest this is a reflection of  
 579 different  $I_\alpha$  values.

To explore this point, we repeated the simulations for the field (A), with  $\alpha = 0.025$ , which sets  $I_\alpha = 160$ , the same for the field (B) and (C) simulations. For brevity, we focus only on the results with variance of  $\sigma_Y^2 = 4$ , although all other cases were considered also.

Fig. 10 also includes the results of  $\sigma_t^2$  against  $\beta$  from these simulations (green squares).

These points behave much like those of field (B) and (C), i.e. a regime close to  $\sigma_t^2 \propto \beta^2$ .

Fig. 11 compares the original BTCs and peak distributions to the new ones (in red).

The results indicate that local dispersivity plays an important role in the distribution of arrival times, but not on the phenomenon relating to BTC slope:

- Fig. 10 suggests a reduction of  $\alpha$  yields a reduction in  $\beta$  (the BTCs tend to have less persistent tailing and thus asymmetry), while the 2D peak spread varies quite little.

This can be seen in fig. 11, where the red ( $I_\alpha = 160$ ) BTCs are narrower than their black ( $I_\alpha = 16$ ) counterparts, while the dots reflecting the 2D peaks display qualitatively similar scatter. This behavior indicates that effects of transverse dispersivity may not be negligible for the development of anomalous behavior in radially convergent transport in 3D systems.

- From Fig. 11 we note that tailing occurs over a narrower range of times, but it does seem that the tail slope is not strongly influenced by  $\alpha$ ; this means that, likely, the slope is more controlled by stratification and connectivity rather than by local dispersion, and transverse dispersivity may not be negligible for the development of PL-like slopes on BTCs. For R1, the qualitative behavior  $\hat{p}(t) \sim t_c^{-1}$  at later times is still somewhat visible in the new BTC with low  $\alpha$  (red curve), even if the "length" of this tail is much shorter than for the simulation with a larger  $\alpha$ . Discrepancies between the breakthrough curves diminish as the normalized injection distances increases suggesting less sensitivity to local

603 dispersivity values, probably due to comparable heterogeneity sampling by the particles  
 604 over very large times.

### 4.3. What does $\hat{p}(t) \sim t^{-1}$ scaling mean?

605 To explain why the specific power-law behavior with  $m = 1$  arises on depth-integrated  
 606 BTCs, let us first consider why this occur on the slope of the peaks of 2D BTCs. We  
 607 already noticed from fig. 3 that the architecture of the tracer, once it has been injected  
 608 into the well, is stratified, due to the flux-weighted scheme. Such stratification is due to the  
 609 existence of hydraulic heterogeneities, that condition (a) the mass injected in each layer,  
 610 which depends exclusively on the flow velocities at the cells located along the injection  
 611 column and (b) the mean travel time along each horizon.

612 In a perfectly stratified homogeneous medium ( $e = I_z/I_x \rightarrow 0$ ), each layer acts indepen-  
 613 dently. This is strictly valid assuming negligible transverse dispersion. In this limit case,  
 614 convergent radial transport in each layer can be approximated by the analytical solution  
 615 of *Welty and Gelhar* [1994] (their Eq. 26), which after some manipulation, allows us to  
 616 estimate the peak concentration ( $c_{pk}$ ) as

$$c_{pk} = \frac{M}{2Qt_{pk}} \left( \frac{4}{3}\pi \frac{a_L}{r} \right), \quad (10)$$

617 where  $\alpha_L$  is the longitudinal dispersivity. This solution is valid for advection-dominated  
 618 transport ( $r/a_L > 20$ ). This result highlights that the maximum concentration in each  
 619 layer scales linearly with the layer-specific injected mass  $M$  and inversely with the dis-  
 620 charge rate  $Q$ .

For the 2D-BTCs, the injected mass in all realizations is equal. Thus the peak concentrations are governed by  $Q$  and  $t_{pk}$ .  $Pe$  is constant for a given injection distance. Hence, from (10) we can say that

$$c_{pk}t_{pk} \sim \psi \frac{M}{Q}, \quad (11)$$

where  $\psi$  is a constant. Note that this relationship can and is often used to design the total mass of solute tracer to be injected during experiments.

Now, how do we translate this concept to our three-dimensional models and to depth-integrated BTCs? Assuming again a perfectly stratified homogeneous medium, for a given layer and due to boundary conditions (flux-averaged injection) the ratio  $M/Q$  should be constant. Thus, in each layer the condition

$$c_{pk} \sim t_{pk}^{-1} \quad (12)$$

should be satisfied. Under some conditions (that we identified to be controlled by the parameters  $\sigma_Y^2$ ,  $\sigma_t^2$  and  $r_\lambda$ ), the 3D solute transport becomes so highly stratified that each layer acts separately and the final shape is eventually similar to a PL with  $m = 1$  (independent of the statistical distribution of  $Y$ , and also despite the fact that the three-dimensional flow solution allows for transverse dispersion). The further away from these conditions, the more the solution deteriorates.

This explains why we found a universal scaling PL with slope  $m = 1$  only for certain fields, and why it is different than  $m = 2$  proposed by the *Becker and Shapiro [2003]* model. Their universal BTCs with PL slope  $m = 2$  were obtained as a convolution of single BTCs from individual channels plus the advection-dispersion equation; however, they assumed

640 individual channels acting independently, that in each channel  $M$  is proportional to the  
 641 cube of the mean channel size, and also that the mean advection time was proportional to  
 642 the square of the mean channel aperture. Here, we do not have such conditions, since our  
 643 solution for single 'channel' (horizon) follows *Welty and Gelhar* [1994] solution, as stated  
 644 previously.

## 5. Conclusions

645 We have studied the development of heavy-tailed BTCs in heterogeneous porous media  
 646 using a numerical approach, based on single realizations of flow and transport in stochas-  
 647 tic multigaussian log-normal hydraulic conductivity fields. We used a three-dimensional  
 648 approach under convergent radial flow, to reflect realistic conditions often used in real  
 649 tracer tests. We note that despite this very practical application, the topic appears to  
 650 have received relatively little attention in the literature to date.

651 This work focused on the development of heavy-tailed breakthrough curves, and in  
 652 particular on the physical mechanisms that determine power-law tails with unit slope at  
 653 late time (i.e. after the concentration peak has elapsed), which have been observed in real  
 654 tests.

655 The first conclusion of this work was that in realistic three-dimensional settings, the  
 656 late-time distribution of the concentrations observed in convergent flow field tracer tests  
 657 is mainly controlled by the degree of stratification of the solute. For a given random field  
 658 with well defined geostatistical properties, different late-time behaviors are observed for  
 659 breakthrough curves obtained from different injection locations.

660 We note that we observe BTC scaling at late time with unit slope power-law behavior  
 661 when the following conditions are met:

- 662     1. large vertical variability of the connectivity for the layers making up the 3D forma-  
663     tion;
- 664     2. disordered systems (with mid to high variance);
- 665     3. injection distance comparable with the planar horizontal integral scale of the het-  
666     erogeneity;

667     Conditions 1 and 2 are highly correlated. We demonstrated that a possible reason for  
668     this is that the maximum concentrations of breakthrough curves under homogeneous flow  
669     conditions scale inversely with arrival time of the peak value. When these conditions were  
670     not or only partially fulfilled, BTCs no longer showed PL distribution, but they could still  
671     display heavy-tailing.

672     This work suggested that full three-dimensional models are required to reproduce skewed  
673     BTCs similar to the ones observed in field settings. Tailing does not naturally occur in  
674     our 2D transport simulations. Based on all of this we hypothesized that the nature of  
675     memory functions for large scale effective models of such systems will depend heavily on  
676     the vertical architecture and connectivity patterns between the injection location and the  
677     pumping well.

## 6. Acknowledgments

678     We thank A. Bellin and two anonymous reviewers for their useful suggestions and crit-  
679     icisms that have sensibly helped to improve the quality of this manuscript. We also  
680     acknowledge the discussions with A. Fiori and F.P.J. de Barros on some aspects of this  
681     research. This work has been supported by the Spanish Ministry of Science and Innovation  
682     through the projects Consolider-Ingenio 2010 CSD2009-00065 and FEAR CGL2012-38120.

<sup>683</sup> DP acknowledges the funding provided by the Spanish Ministry of Education through the  
<sup>684</sup> FPU-MED 2009 Scholarship program. DB was supported by NSF grant EAR-1113704.

## References

- 685 Bear, J. (1972), *Dynamics of fluids in porous media*, Elsevier, New York.
- 686 Becker, M., and A. M. Shapiro (2000), Tracer transport in fractured crystalline rock:  
687 Evidence of nondiffusive breakthrough tailing, *Water Resour. Res.*, *36*, 1677–1686.
- 688 Becker, M., and A. M. Shapiro (2003), Interpreting tracer breakthrough tailing from  
689 different forced-gradient tracer experiment configurations in fractured bedrock, *Water  
690 Resources Research*, *39*(1), W1014.
- 691 Bellin, A., and Y. Rubin (2004), On the use of peak concentration arrival times for the  
692 inference of hydrogeological parameters, *Water Resources Research*, *40*(7), 1–13, doi:  
693 10.1029/2003WR002179.
- 694 Bianchi, M., C. Zheng, G. Tick, and S. Gorelick (2011), Investigation of small-scale pref-  
695 erential flow with a forced-gradient tracer test, *Ground Water*, *49*(4), 503–514, doi:  
696 10.1111/j.1745-6584.2010.00746.x.
- 697 Bijeljic, B., and M. J. Blunt (2006), Pore-scale modeling and continuous time random  
698 walk analysis of dispersion in porous media, *Water Resources Research*, *42*, W01,202,  
699 doi:10.1029/2005WR004578.
- 700 Bohling, G. C., G. Liu, S. J. Knobbe, E. C. Rebulet, D. W. Hyndman, P. Dietrich,  
701 and J. J. Butler J.R. (2012), Geostatistical analysis of centimeter-scale hydraulic con-  
702 ductivity variations at the MADE site, *Water Resources Research*, *48*, W02,525, doi:  
703 10.1029/2011WR010791.
- 704 Bolster, D., F. J. Valdes-Parada, T. Le Borgne, M. Dentz, and J. Carrera (2011), Mixing  
705 in confined stratified aquifers, *Journal of Contaminant Hydrology*, *120*-*121*, 198–212.

- 706 Carrera, J., X. Sanchez-Vila, I. Benet, A. Medina, G. Galarza, and J. Guimerà (1998),  
707 On matrix diffusion: formulations, solution methods and qualitative effects., *Hydrogeol.*  
708 *J.*, 6, 178–190.
- 709 Chen, J.-S., C.-W. Liu, H.-T. Hsu, and C.-M. Liao (2003), A Laplace transform power  
710 series solution for solute transport in a convergent flow field with scale-dependent dis-  
711 persions, *Water resources research*, 39(8), 1229.
- 712 Dagan, G. (1989), *Flow and Transport in Porous Formations*, Springer-Verlag, Berlin.
- 713 Dentz, M., and D. Bolster (2010), Distribution-versus correlation-induced anomalous  
714 transport in quenched random velocity fields , *Physical Review Letters*, 105, 244301  
715 doi:10.1103/PhysRevLett.105.244301.
- 716 Dentz, M., and B. Berkowitz (2003), Transport behavior of a passive solute in continuous  
717 time random walks and multirate mass transfer, *Water Resour. Res.*, 39(5), 1111–1131,  
718 doi:10.1029/2001WR001163.
- 719 Fernàndez-Garcia, D. (2003), Scale-dependence of non-reactive and sorptive transport  
720 parameters estimated from radial and uniform flow tracer tests in heterogeneous for-  
721 mations: experimental and numerical inverstigations., Ph.D. thesis, Colorado School of  
722 Mines.
- 723 Fernàndez-Garcia, D., and X. Sanchez Vila (2011), Optimal reconstruction of concentra-  
724 tions, gradients and reaction rates from particle distributions, *Journal of Contaminant*  
725 *Hydrology*, 120-121, 99–114.
- 726 Fernàndez-Garcia, D., T. H. Illangasekare, and H. Rajaram (2004), Conservative and  
727 sorptive forced-gradient and uniform flow tracer tests in a three-dimensional laboratory  
728 test aquifer, *Water Resources Research*, 40, W10,103, doi:10.1029/2004WR003112.

- 729 Fernàndez-Garcia, D., H. Rajaram, and T. H. Illangasekare (2005), Assessment of the pre-  
730 dictive capabilities of stochastic theories in a three-dimensional laboratory test aquifer:  
731 Effective hydraulic conductivity and temporal moments of breakthrough curves, *Water  
732 Resources Research*, 41, W04,002, doi:10.1029/2004WR003523.
- 733 Fernàndez-Garcia, D., P. Trinchero, and X. Sanchez-Vila (2010), Conditional stochastic  
734 mapping of transport connectivity, *Water Resour. Res.*, 46, W10,515.
- 735 Fiori, A., and I. Jankovic (2012), On preferential flow, channeling and connectivity in het-  
736 erogeneous porous formations, *Mathematical Geology*, 44, 133–145, doi:10.1007/s11004-  
737 011-9365-2.
- 738 Fiori, A., I. Jankovic, and G. Dagan (2006), Modeling flow and transport in highly hetero-  
739 geneous three-dimensional aquifers: Ergodicity, gaussianity, and anomalous behavior-  
740 2. approximate semianalytical solution, *Water Resources Research*, 42, W06D13, doi:  
741 10.1029/2005WR004752.
- 742 Flach, G. (2012), Relationship between dual-domain parameters and practical character-  
743 ization data, *Ground Water*, 50(2), 216–229.
- 744 Fogg, G. E. (1986), Groundwater-flow and sand body interconnectedness in a  
745 thick,multiple-aquifer system, *Water Resources Research*, 11(5), 679–694.
- 746 Gelhar, L., and M. A. Collins (1971), General analysis of longitudinal dispersion in nonuni-  
747 form flow, *Water Resources Research*, 7(6), 1511–1521.
- 748 Gelhar, L., C. Welty, and K. Rehfeldt (1992), A critical review of data on field-scale  
749 dispersion in aquifers, *Water Resources Research*, 28, 1955–1974.
- 750 Gomez-Hernandez, J. J., and X. H. Wen (1998), To be or not to be multi-Gaussian? a  
751 reflection on stochastic hydrogeology, *Advances in Water Resources*, 21(1), 47–61.

- 752 Gouze, P., T. Le Borgne, R. Leprovost, G. Lods, T. Poidras, and P. Pezard (2008),  
753 Non-Fickian dispersion in porous media: 1. Multiscale measurements using single-  
754 well injection withdrawal tracer tests, *Water Resources Research*, 44, W06,426, doi:  
755 10.1029/2007WR006278.
- 756 Harbaugh, A. W., E. R. Banta, M. C. Hill, and M. G. McDonald (2000), Modflow-2000,  
757 the u.s. geological survey modular ground-water model – user guide to modularization  
758 concepts and the ground-water flow process, *Tech. rep.*, U.S. Geological Survey Open-  
759 File Report 00-92, 121 p.
- 760 Hoehn, E., J. Eikenberg, T. Fierz, W. Drost, and E. Reichlmayr (1998), The grimsel  
761 migration experiment : field injection-withdrawal experiments in fractured rock with  
762 sorbing tracers, *Journal of Contaminant Hydrology*, 34, 85–106.
- 763 Knudby, C., and J. Carrera (2006), On the relationship between indicators of geostatis-  
764 tical, flow and transport connectivity, *Advances in Water Resources*, 28(4), 405 – 421,  
765 doi:DOI: 10.1016/j.advwatres.2004.09.001.
- 766 Le Borgne, T., M. Dentz, D. Bolster, J. Carrera, J. R. de Dreuzy, and P. Davy (2010),  
767 Non-fickian mixing: Temporal evolution of the scalar dissipation rate in heterogeneous  
768 porous media, *Advances in Water Resources*, 33(12), 1468–1475.
- 769 Levy, M., and B. Berkowitz (2003), Measurement and analysis of non-fickian dispersion  
770 in heterogeneous porous media, *Journal of Contaminant Hydrology*, 64(3-4), 203–226.
- 771 MacKay, D. M., D. L. Freyberg, P. V. Roberts, and J. A. Cherry (1986), A nat-  
772 ural gradient experiment on solute transport in a sand aquifer, 1, Approach and  
773 overview of plume movement, *Water Resources Research*, 22(13), 2017–2029, doi:  
774 10.1029/WR022i013p02017.

- 775 McKenna, S., L. Meigs, and R. Haggerty (2001), Tracer tests in a fractured dolomite. 3.  
776 double-porosity, multiple-rate mass transfer processes in convergent flow tracer tests.,  
777 *Water Resour. Res.*, 37(5), 1143–1154.
- 778 Moench, A. (1989), Convergent radial dispersion: A laplace transform solution for aquifer  
779 tracer testing, *Water Resour. Res.*, 25(3), 439–447.
- 780 Parker, J. C., and M. T. Van Genuchten (1984), Flux-averaged and volume-averaged  
781 concentrations in continuum approaches to solute tranport, *Water Resources Research*,  
782 20(7), 866–872.
- 783 Ptak, T., and G. Schmid (1996), Dual-tracer transport experiments in a physically and  
784 chemically heterogeneous aquifer material: effective transport parameters and spatial  
785 variability, *Journal of Hydrology*, 183(1-2), 117–138.
- 786 Ptak, T., M. Piepenbrink, and E. Martac (2004), Tracer tests for the investigation of  
787 heterogeneous porous media and stochastic modelling of flow and transport - a review  
788 of some recent developments, *Journal of Hydrology*, 294, 122–163.
- 789 Remy, N., A. Boucher, and J. Wu (2009), *Applied Geostatistics with SGeMS. A User's  
790 Guide*, new york cambridge university press. ed.
- 791 Renard, P., and D. Allard (2013), Connectivity metrics for subsurface flow and transport,  
792 *Advances in Water Resources*, 51, 168–196, doi:10.1016/j.advwatres.2011.12.001.
- 793 Riva, M., X. Sanchez-Vila, A. Guadagnini, M. De Simoni, and M. Willmann  
794 (2006), Travel time and trajectory moments of conservative solutes in two-  
795 dimensional convergent flows., *Journal of Contaminant Hydrology*, 82(1-2), 23, doi:  
796 10.1016/j.jconhyd.2005.06.014.

- 797 Riva, M., A. Guadagnini, D. Fernandez-Garcia, X. Sanchez-Vila, and T. Ptak (2008),  
798 Relative importance of geostatistical and transport models in describing heavily tailed  
799 breakthrough curves at the Lauswiesen site, *Journal of Contaminant Hydrology*, 101,  
800 1–13, doi:10.1016/j.jconhyd.2008.07.004.
- 801 Salamon, P., D. Fernàndez-Garcia, and J. Gomez-Hernandez (2006), Modeling mass trans-  
802 fer processes using random walk particle tracking, *Water Resour. Res.*, 42, W11,417,  
803 doi:10.1029/2006WR004927.
- 804 Salamon, P., D. Fernàndez-Garcia, and J. Gomez-Hernandez (2007), Modeling tracer  
805 transport at the made site: The importance of heterogeneity, *Water Resources Research*,  
806 43, W08,404, doi:10.1029/2006WR005522.
- 807 Sanchez-Vila, X., and J. Carrera (2004), On the striking similarity between the mo-  
808 ments of breakthrough curves for a heterogeneous medium and a homogeneous  
809 medium with a matrix diffusion term, *Journal of hydrology*, 294(1-3), 164/175, doi:  
810 10.1016/j.jhydrol.2003.12.046.
- 811 Sanchez-Vila, X., J. Carrera, and J. Girardi (1996), Scale effects in transmissivity, *Journal*  
812 *of Hydrology*, 183(1-2), 1–22.
- 813 Trinchero, P., X. Sanchez-Vila, and D. Fernàndez-Garcia (2008), Point-to-point connec-  
814 tivity, an abstract concept or a key issue for risk assessment studies?, *Advances in Water*  
815 *Resources*, 31(12), 1742–1753, doi:10.1016/j.advwatres.2008.09.001.
- 816 Welty, C., and L. W. Gelhar (1994), Evaluation of longitudinal dispersivity from nonuni-  
817 form flow tracer tests, *Journal of Hydrology*, 153(1), 71–102.
- 818 Willmann, M., J. Carrera, and X. Sanchez-Vila (2008), Transport upscaling in heteroge-  
819 neous aquifers: What physical parameters control memory functions?, *Water Resour.*

820      *Res.*, 44, W12,437, doi:10.1029/2007WR006531.

821      Zinn, B., and C. F. Harvey (2003), When good statistical models of aquifer heterogeneity  
822      go bad: A comparison of flow, dispersion and mass transfer in connected and multi-  
823      variate gaussian hydraulic conductivity fields, *Water Resources Research*, 39(3), 1051,  
824      doi:10.1029/2001WR001146.

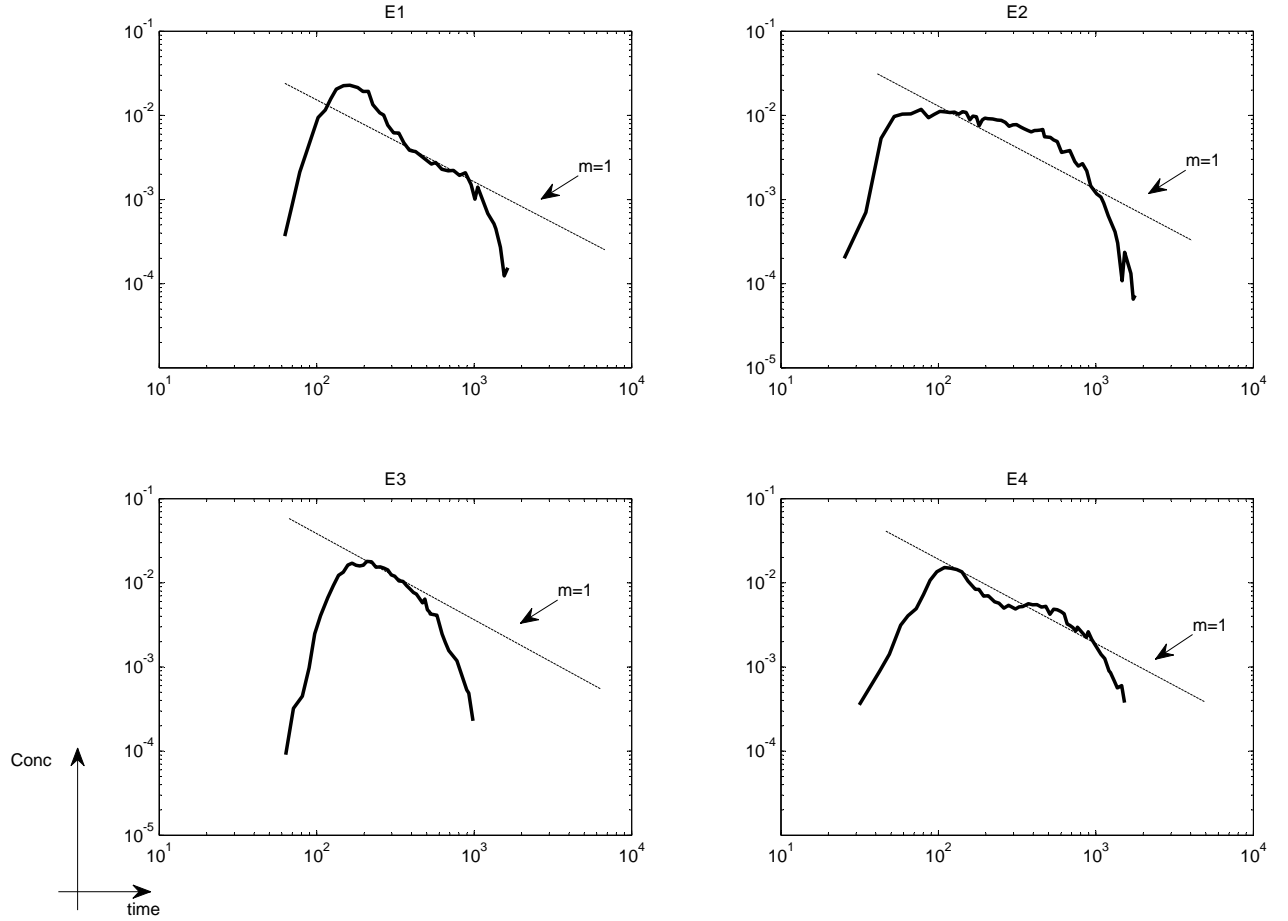


**Figure 1.** Four of the experimental BTCs obtained by *Fernàndez-Garcia et al.* [2004] during CFTT in heterogeneous 3D tank. Notice that the part of the BTCs showing heavy-tailed distribution scale following  $c \sim t^{-1}$  (at E1 and at E4), while at E2 and E3 the shape is more symmetric. The injecting location varies within the 3D tank, keeping the radial distance from the well ( $r_\lambda \approx 2$ )

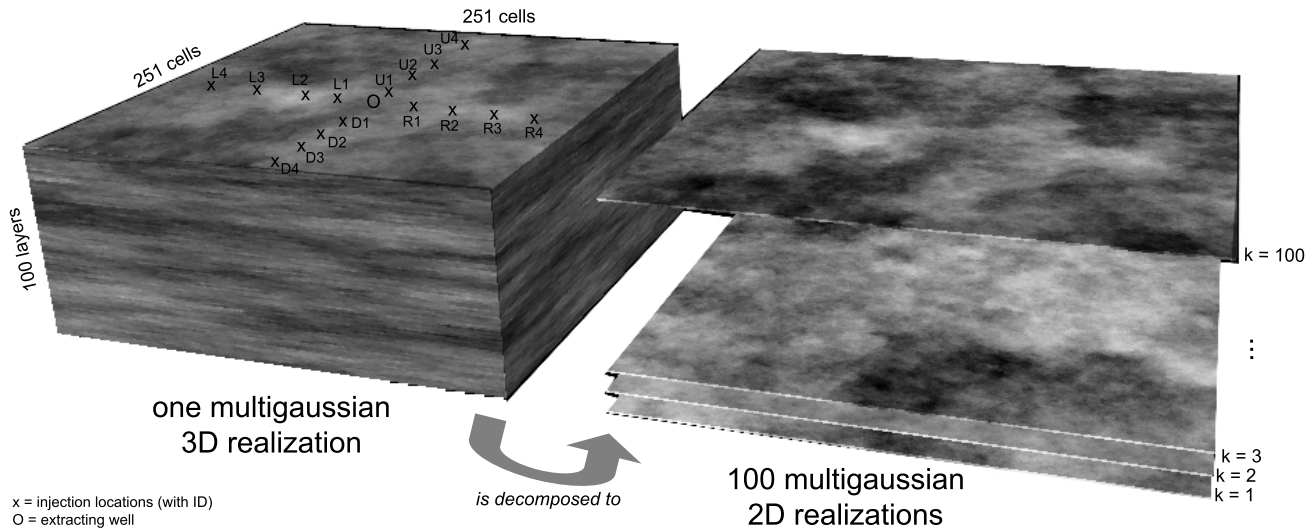


**Figure 2.** On the left, the 3D anisotropic field (B) used in the simulations, along with the position of the injection locations at various radial distances and angles around the well. On the right, schematic decomposition of a 3D field into 100 layers, each of them representing a 2D field with the same planar spatial correlation as the 3D original counterpart.

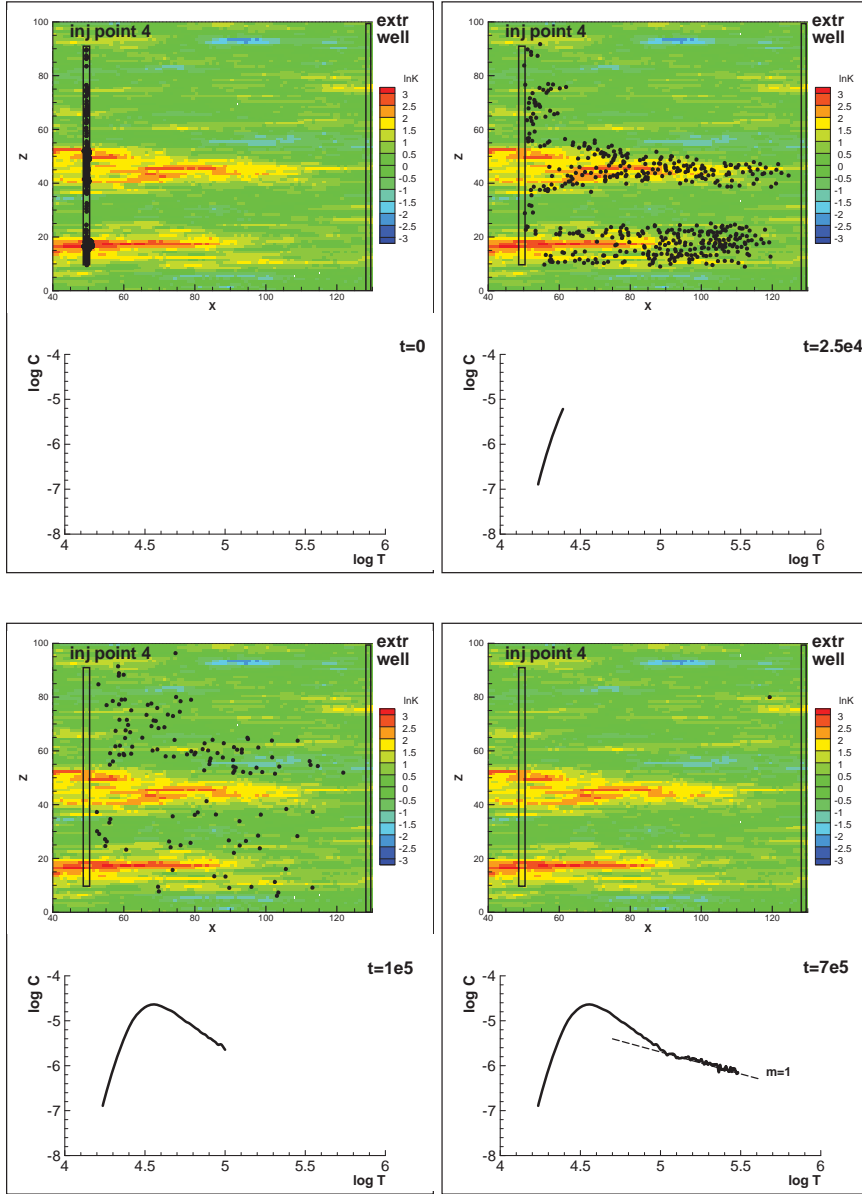


**Figure 3.** (In color online) Particle displacement at different temporal steps during the simulation of a CFTT in the anisotropic field (B) with  $\sigma_Y^2 = 4$ , after injecting from position L4. In the upper plots, particles are plotted along with the distribution of log-transformed hydraulic conductivities,  $Y$ , at the central section of the domain. In the bottom, the evolution of the BTC estimated as 'depth-integrated' particle mass density at the extraction well.

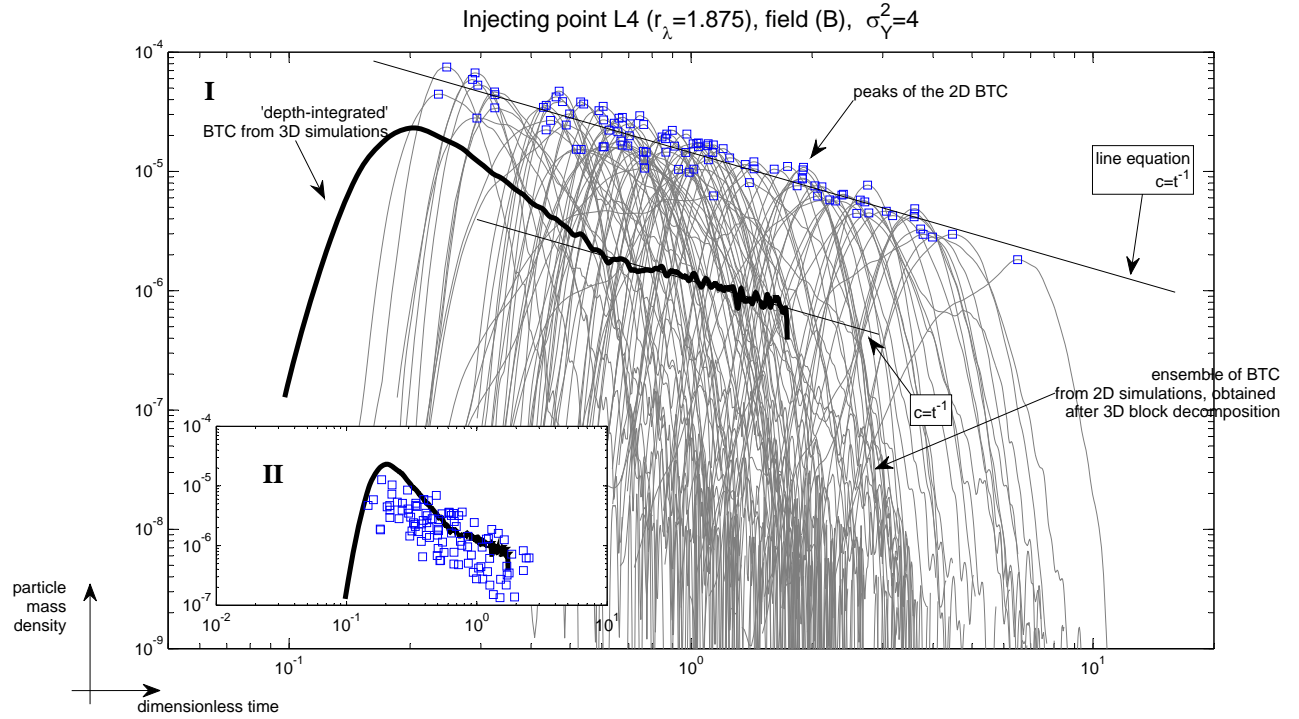


**Figure 4.** Superposition of particles pdfs (BTC) obtained after injecting at L4 in the the anisotropic field (B) with  $\sigma_Y^2=4$  and  $r_\lambda = 1.875$ . 3D BTC is plotted with a dark strong line. 2D BTC from 'layer injection' are plotted with gray colors. A red 2D curve is plotted to emphasize one of the rare examples of heavy-tailed 2D BTC. The peaks of the 2D are marked in blue. Two lines with slope  $c \sim t^{-1}$  are overlapping the 2D peak cloud and the late-time of the 3D BTCs to highlight this late-time scaling behavior.

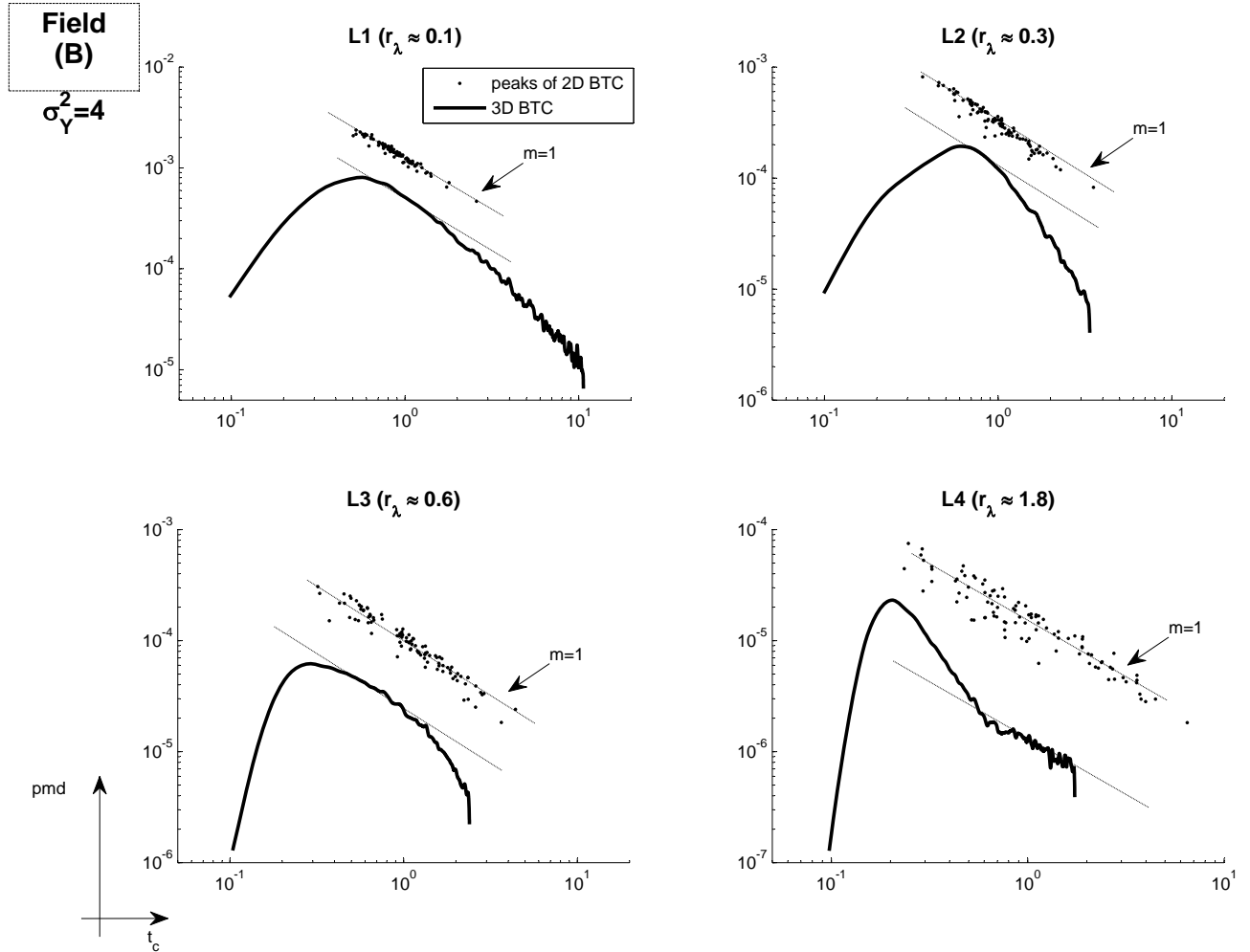


**Figure 5.** 3D BTCs (and relative peak distributions) obtained after injecting in the anisotropy field (B) with  $\sigma_Y^2=4$ , at L-points. Notice that the behavior  $\hat{p}(t) \sim t_c^{-1}$  can be fitted only at L4 ( $r_\lambda \approx 1.8$ ), while the other locations display a more symmetric behavior.

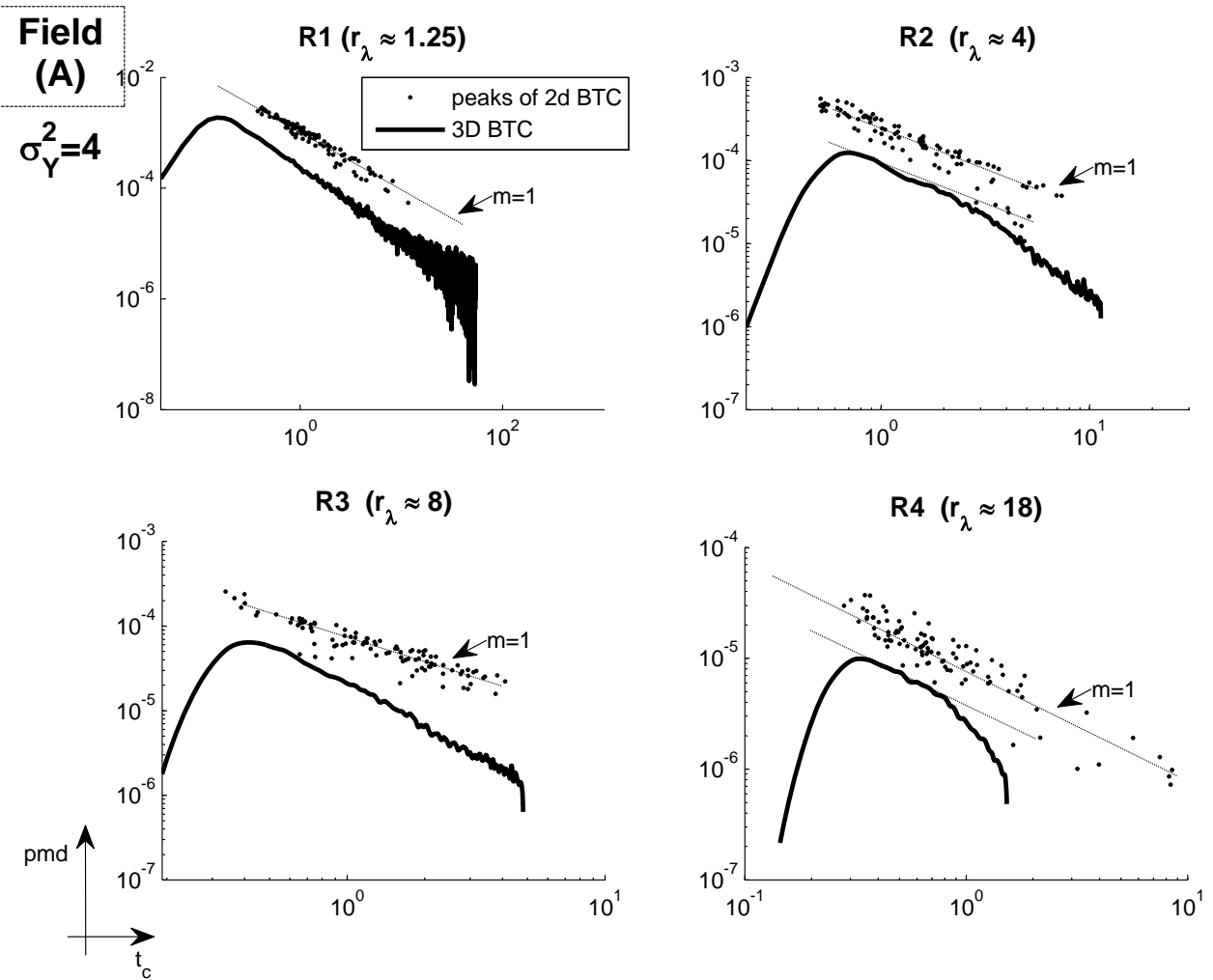


**Figure 6.** 3D BTCs (and relative peak distributions) obtained after injecting in the isotropic field (A) with  $\sigma_Y^2=4$ , at R-points. Notice that the behavior  $\hat{p}(t) \sim t_c^{-1}$  is very similar to the 3D BTC slope at L1 ( $r_\lambda \approx 1.25$ ), but tend to diverge as long as the injection distance increases. At R4, the BTCs is more symmetric.

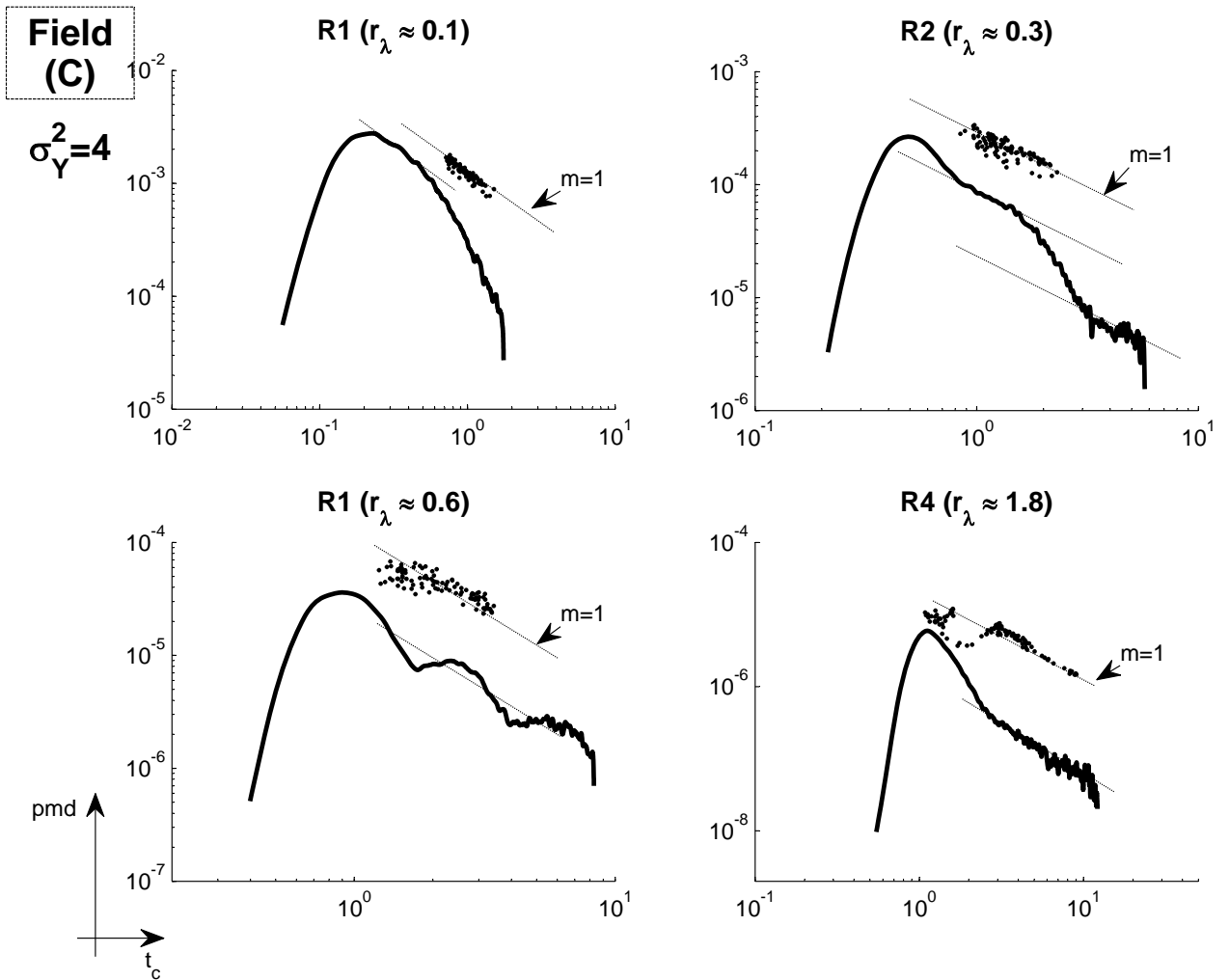


**Figure 7.** 3D BTCs (and relative peak distributions) obtained after injecting in the anisotropy field ( $\text{C}$ ) with  $\sigma_Y^2=4$ , at R-points. Notice that the behavior  $\hat{p}(t) \sim t_c^{-1}$  can be fitted at L4 ( $r_\lambda \approx 1.8$ ). From R1 to R4, the 3D BTCs increasingly tend to heavy-tailed distributions; at R2 and R3, a PL behavior with  $m = 1$  can be inferred at different intermediate portions of the BTCs.

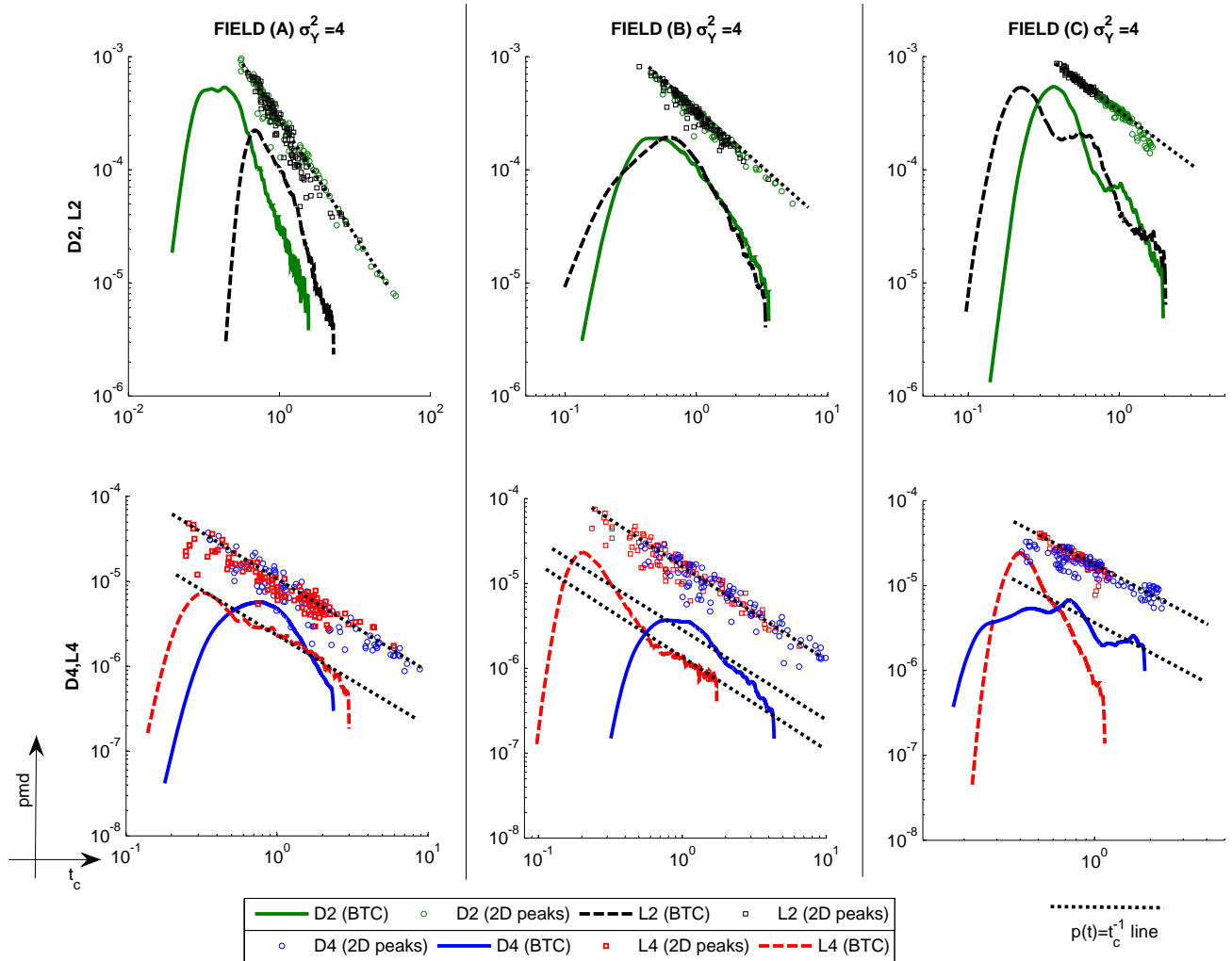


**Figure 8.** (In color online) 3D BTCs (and relative peak distributions) after injecting in the three fields A,B,C with  $\sigma_Y^2=4$ , at different locations. The line indicate which BTCs display a behavior like  $\hat{p}(t) \sim t_c^{-1}$ .

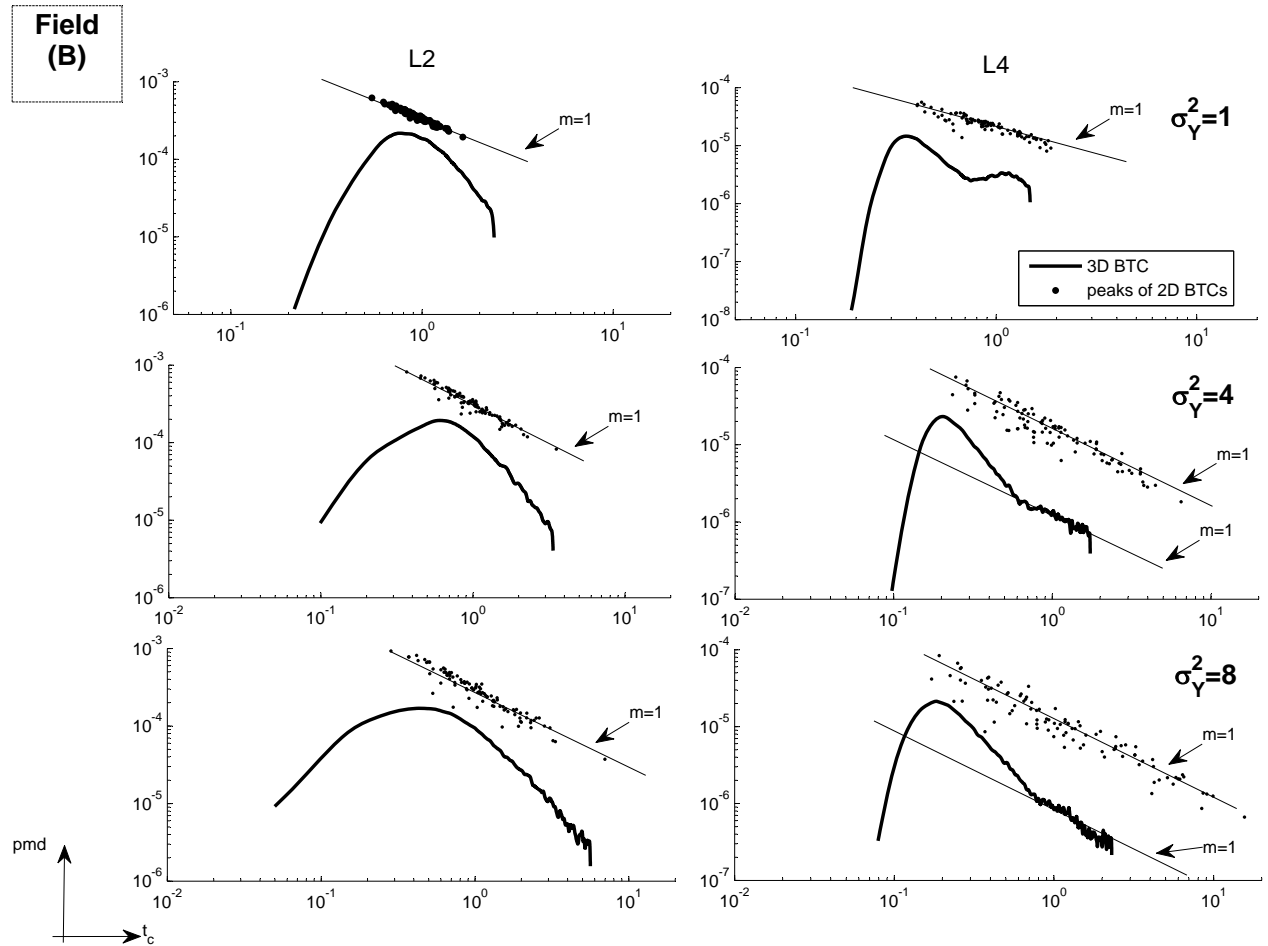


**Figure 9.** 3D BTCs (and relative peak distributions) for the anisotropic field (B) for variable variance ( $\sigma_Y^2=1,4,8$ , respectively from top to bottom of the plot), at two injection locations, L2 and L4. Note that BTC tends to scale as a PL with  $m \approx 1$  for L4 in case of variance  $\sigma_Y^2 = 4$  and 8, which also show distribution of 2d peaks more spread than in the case where  $m$  is not found close to the unit.

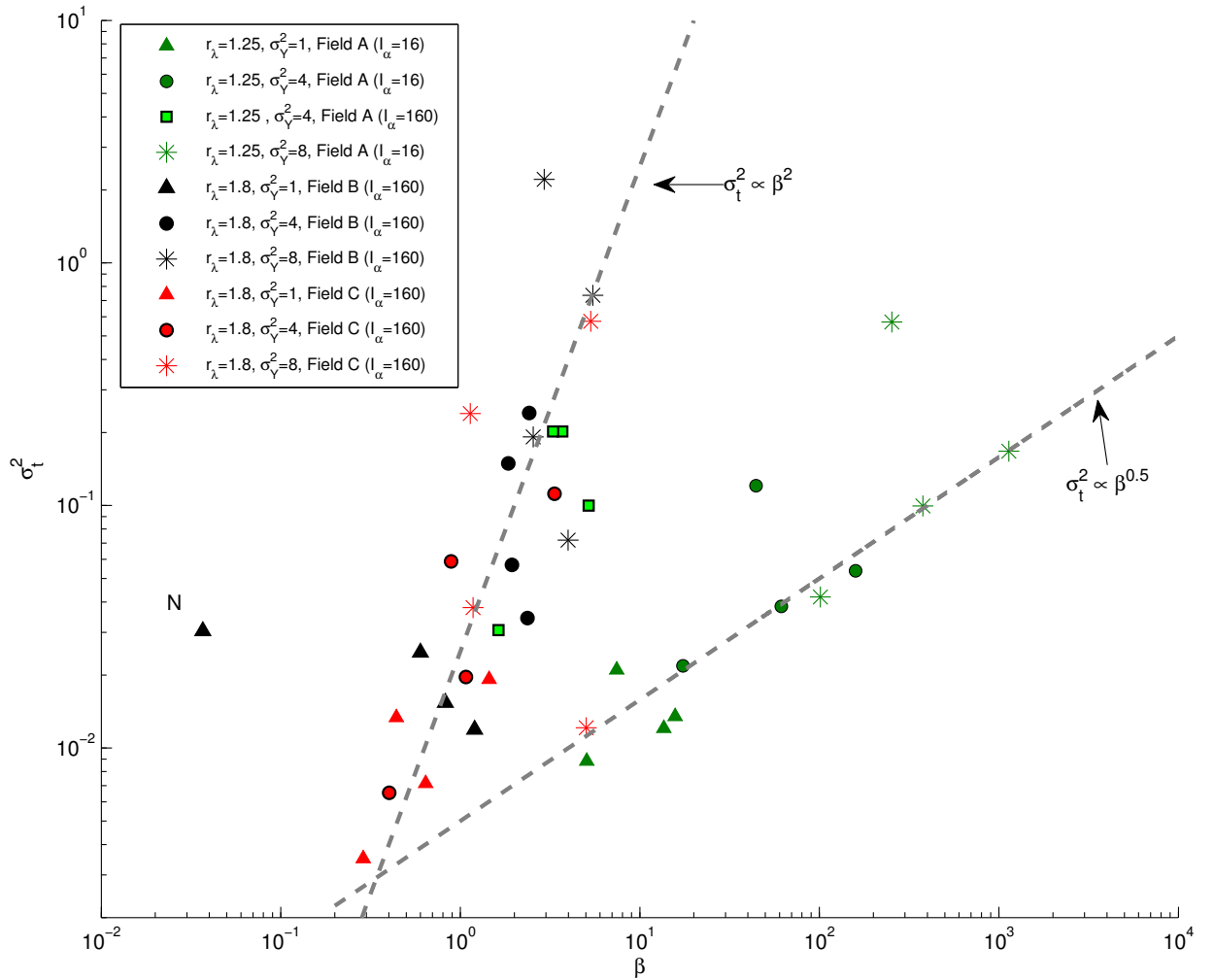


**Figure 10.** (In color online) Relationship between 2D-peak spreading,  $\sigma_t^2$ , and degree of tailing of 3D BTCs,  $\beta$ , measured for field (A),(B) and (C) using normalized injection distance  $r_\lambda \approx 1$  and different variances  $\sigma_Y^2$ . We note that all the points having  $I_\alpha = 160$  are collinear with a power law correlation with a slope of 2, while points having  $I_\alpha = 16$  are collinear with a power law correlation with a slope of 0.5.

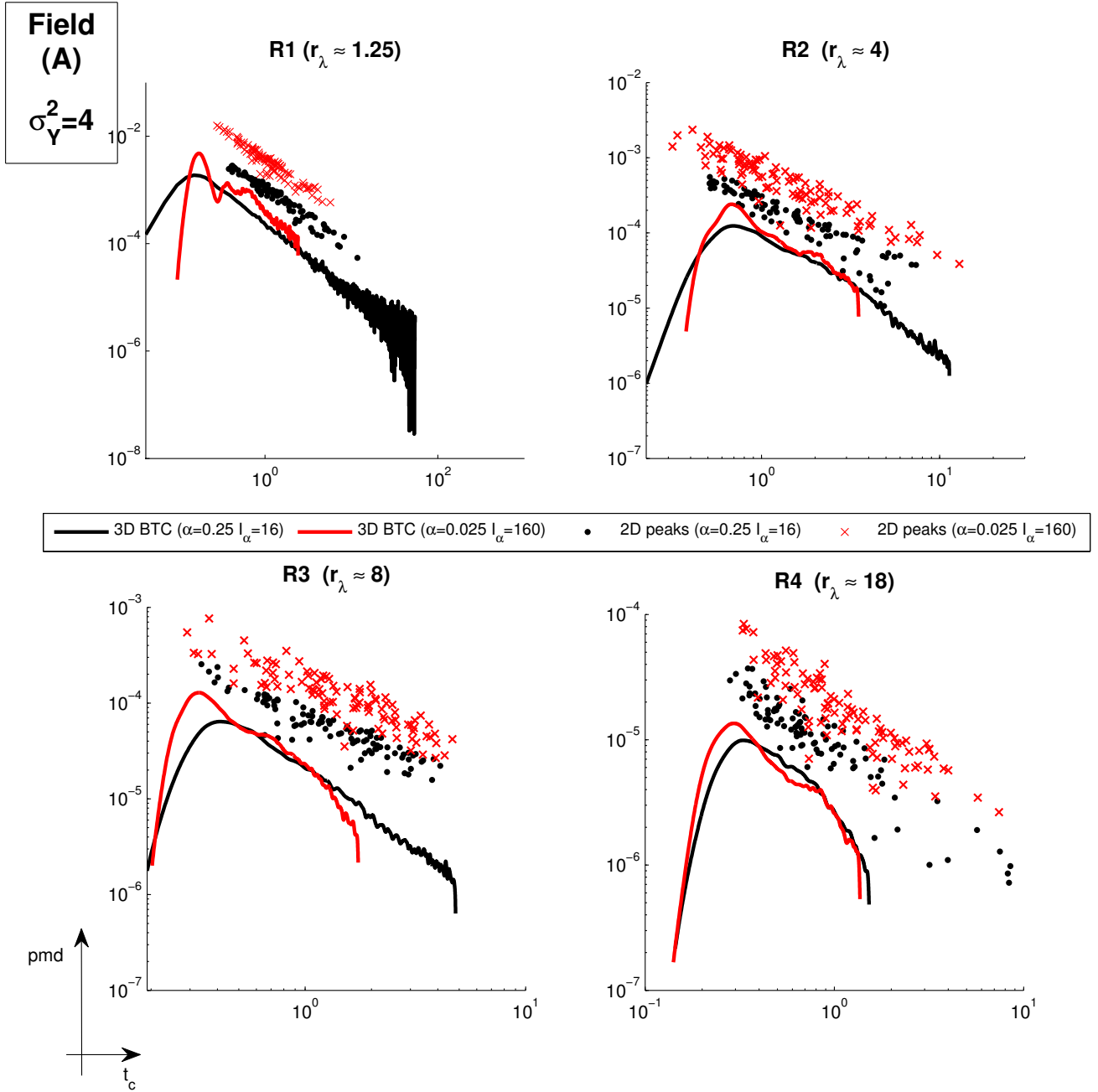


**Figure 11.** Comparison between 3D BTCs (and relative peak distributions) obtained after injecting in the isotropic field (A) with  $\sigma_Y^2=4$  at R-points, with two different local dispersivity ( $\alpha$ ) values and consequently with two different  $I_\alpha$  ratios.